Fast dynamics of an eel-like robot, comparisons with Navier-Stokes simulations

Frederic Boyer[1], Mathieu Porez[2], Alban Leroyer[3] and Michel Visonneau[4]

Technical Report of École des Mines de Nantes and Institut de Recherche en Communication et Cybernétique de Nantes.

Report No. : 07/9/Auto

Abstract

This article proposes a dynamic model of the swim of elongated fishes suited to the on-line control of bio-mimetic eel-like robots. The approach is analytic and can be considered as an extension of the original reactive "Large-Elongated-Body-Theory" of Lighthill to the three dimensional self propulsion augmented of a resistive empirical model. While all the mathematical fundamentals are detailed in [1], this article essentially focuses on the numerical validation and calibration of the model and the study of swimming gaits. The proposed model is coupled to an algorithm allowing us to compute the motion of the fish head and the field of internal control torque from the knowledge of the imposed internal strain fields. Based on the Newton-Euler formalism of robots dynamics, this algorithm works faster than real time. As far as precision is concerned, many tests obtained with several planar and three dimensional gaits are reported and compared (in the planar case) with a Navier-Stokes solver, devoted until today to the planar swim. The comparisons obtained are very encouraging since in all the cases we tested, the differences between our simplified and reference simulations do not exceed ten per cent.

Keywords

Bio-Robotics, underwater vehicle, eel-like robots, swim dynamics.

1 Introduction

In this article, we present some of the results of a multidisciplinary research project where the purpose is to study, design, build and control an eel-like robot capable of swimming in three dimensions (see figure 1). As it has been noted in the Bio-Robotics community, eel-like robots are a promising perspective for improving the efficiency and manoeuverability of modern day underwater vehicles [2]. From the mechanical design point of view, the good performance of these future under-water bio-mimetic vehicles are due to the high redundancy of their internal kinematics with respect to the six dimensional task consisting in moving their head. Until today, two kinds of fish have essentially focused the attention of robotic researchers : the "carangiform" and "anguilliform swimmers". Initially introduced by Breder [3], this classification of fish locomotion is based on the wavelength and the amplitude of the propulsive wave traveling along the body of the animal. As far as the propulsion principle is properly concerned, the body undulations generate the thrust by pushing the fluid (with respect to the body) from the head to the caudal

[1]**F. Boyer :** EMN, IRCCyN, La Chantrerie 4, rue Alfred Kastler B.P. 20722 - 44307 Nantes Cedex 3 France. Tel. : +00 33 2 51 85 83 08, Fax : +00 33 2 51 85 83 02, E-mail : frederic.boyer@emn.fr.

[2]**M. Porez :** EMN, IRCCyN, La Chantrerie 4, rue Alfred Kastler B.P. 20722 - 44307 Nantes Cedex 3 France. Tel. : +00 33 2 51 85 83 33, Fax : +00 33 2 51 85 83 02, E-Mail : mathieu.porez@emn.fr.

[3]**A. Leroyer** ECN, LMF, 1 rue de la Noë BP 92101 - 44321 Nantes Cedex 3 France. Tel. : +00 33 2 40 37 16 48, E-mail : alban.leroyer@ec-nantes.fr.

[4]**M. Visonneau** ECN, LMF, 1 rue de la Noë BP 92101 - 44321 Nantes Cedex 3 France. E-mail : michel.visonneau@ec-nantes.fr.

fin where it is shed into the wake. For carangiform swimmers, due to their rigidity, the wave propagation is restricted to the rear third part of the body unlike to the anguilliform swimmers where near 80 % of the body participates in the propulsion. Generally, the anguilliform swimmers are more agile in confined environments but slower in free waters. Moreover, due to their relative simplicity compared to anguilliform swimmers most of the technological devices designed today are inspired by carangiform swimmers (see [4, 5, 6, 7, 8]). These bio-inspired underwater vehicles are most of the time, made up of a single rigid body connected to an actuated tail. Furthermore, the tail internal kinematics have few (less than 4) degrees of freedom and are devoted to the planar swim. However, in [5] and [8], a three dimensional swimming robot is presented where the previous mentioned architecture is provided with two lateral actuated appendages playing the role of pectoral fins. In the article presented here, the copied fish is an anguilliform swimmer as is the eel. The prototype that we are building today (see figures 1(a)-(b)) is a serial assembling of parallel robots [9], each of them introducing a universal joint between two contiguous rigid platforms. These platforms mimic the vertebrae of the animal. However, contrary to the case of a swimming eel in free water, the body can bend in two directions (yaw and pitch) thereby improving the 3-D agility of the robot (see figures 1(a) and 2) in constrained environments.

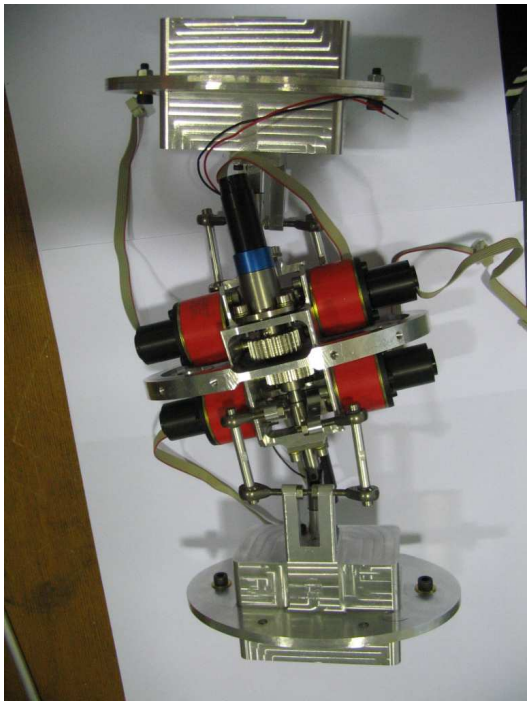

(a) A vertebra.

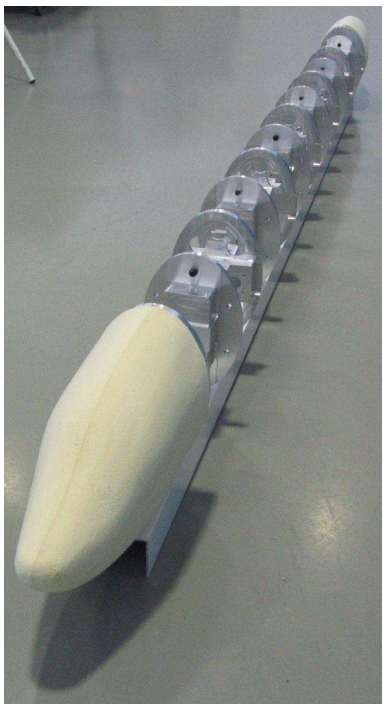

(b) Serial assemblage of vertebrae.

FIG. 1 – Pictures of the prototype.

In the near future, this actuated skeleton will be covered with a flexible organ playing the role of the animal's muscles and skin. This organ will be designed in order to guarantee the continuity of contact with the fluid while preserving the energy resources of the actuators. In order to control such a system, we need simple dynamic models which can be used in real time. This article is directly related to this goal which until today has been a challenging task for researchers involved in bio-mimetic robotics [10].

In its generality, the problem of the dynamic modeling of the swim consists in deriving the laws that rule the following string of causalities : The fish deforms its body. Through its geometry the body imposes unsteady boundary conditions to the fluid flow. This flow exerts on the body boundaries a field of contact forces which produces at the end a wrench that drives the rigid

overall fish motion. Hence we see appear three linked and coupled dynamics.

• The internal dynamics of the body deformations which rule the motion of each body particle with respect to the others.
• The dynamics of the contact forces exerted onto the body boundary and which is in the absolute a consequence of the Navier-Stokes equations of the fluid.
• The dynamics of the overall rigid motions that we name external dynamics since they rule the motion of a rigid reference linked to the fish (for instance its head) with respect to an external Galilean reference frame.

The dynamic modeling of the contact forces (ruled by the dynamics of the ambient medium) is by far, the most complicated of the three problems mentioned above. From Hydrodynamics to Biology and Robotics a very rich literature about the subject has grown these last years. Going further into the details, three great modeling approaches have been proposed depending if they are based on (from the most realistic to the most simple) : 1°) Navier-Stokes dynamics and finite volume elements technics (see [11, 12, 13, 14, 15, 16]), 2°) ideal fluid dynamics and boundary elements methods (see [17, 18, 19, 20]), 3°) analytical fluid mechanics (see [21, 22, 23, 24, 25, 26, 27, 28, 29]). In spite of the increasing performance of embedded computing technologies, it is today impossible to solve the Navier-Stokes equations or even the inviscid fluid equations for on-line control purposes. Hence, analytical modeling seems the most realistic solution yet for robotics control purposes. Historically, Taylor introduced in the 50's, the first analytical model of the fish swim [21]. Devoted to the submarine worms, the solution is based on Stokes equations and models the propulsion through quasisteady lateral drag forces. This model called resistive by Lighthill (see [25]), is used today for studying the swim of small fishes [30]. Eight years after the works of Taylor, Wu [26] and Lighthill [22] independently proposed a model of the fish swim. The "weaving plate model" of Wu considers the fish as a flexible infinite height plate moving in an ideal fluid. From an expansion in perturbations of the potential velocity field (see [31]), Wu computed the hydrodynamics forces exerted onto the plate. This theory has been used by Wolfgang in [18] to study the tuna swim. As far as the Lighthill works are concerned, the Elongated Body Theory (E.B.T.) is based on Slender Body Theory (S.B.T.) of Munk (see [32]) where the three-dimensional flow around an elongated body is approximated by a stratification of planar lateral flows which are then analytically resolved. First developed for fishes enduring small perturbations of their body geometry [22], the E.B.T. was then extended to the case of large amplitude body deformations through the Large Amplitude Elongated Body Theory (L.A.E.B.T.) of [25]. Till today, many researchers in experimental biology use L.A.E.B.T. for computing swimming efficiency [25] or hydrodynamic forces [33, 34]. More recently, these analytical approaches have been enhanced with many results from Geometric Mechanics (see [27, 28, 29]) which take their origin in the Kirchhoff works about Euler-Lagrange equations applied to solid bodies plunged in an ideal fluid [35].

In the article here presented, we propose to exploit and validate the results of [1] where, thanks to the tools of Geometric Mechanics (Lagrangian reduction in particular), the three dynamic modeling problems previously stated (internal, external and contact dynamics) are solved under an analytical simplified form suited to the online control of eel-like robots. From the fluid point of view, the solution proposed is based on the original Elongated Body Theory (E.B.T.) of Lighthill [22, 23, 24, 25], where the propulsion is modeled through the effect of the lateral fluid inertial forces applied along the undulating fish body. As far as the body is concerned, the approach uses a Cosserat beam theory [36] like that of [37], used in the eighties by J.C. Simo in the framework of the "Geometrically Exact Finite Element Method" [38, 39]. In fact, as in [30] where a model of the fish muscles is proposed for planar swim, the eel is here considered as a non-linear beam controlled continuously along its material axis. At the end, the resulting model

turns out to be a generalization of the Large Amplitude Elongated Body Theory (L.A.E.B.T.) of [25] in the following ways : 1°) the L.A.E.B.T. is extended to the three-dimensional swim. 2°) The swimming dynamics are self-propelled and thus the external dynamics of overall rigid motions are solved rather than being imposed. 3°) The internal dynamics of the beam-like fish are also solved in order to compute the torque control law. 4°) The pure reactive model of the Lighthill theory is completed with a Taylor-like resistive model where the dimensionless coefficients are calibrated through comparisons with a Navier-Stokes solver modeling the turbulence [14]. Finally, this solution is based on a fast algorithm recently proposed in [40]. The results are encouraging since for a set of high Reynolds ($\cong 6.10^5$) planar swimming gaits including the straight forward undulation, the turning, and the stopping, the discrepancies between the simplified analytical model and the Navier-Stokes simulations do not exceed 10 percent, while the analytical model is sufficiently fast to be used for on-line control.

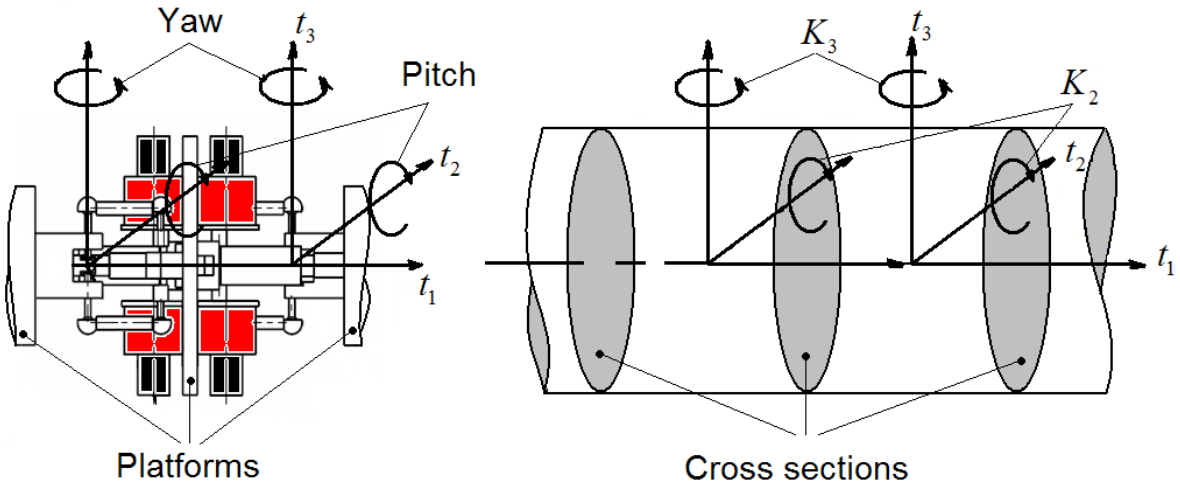

FIG. 2 – From the hybrid (serial/parallel) robot to the continuous beam-like one.

The article is structured as follows. The model of the internal body and contact dynamics (where the fluid is considered as ideal), are presented in section 2 and 3 respectively. In section 4, the previous model, which is nothing but an extension of the reactive L.A.E.B.T. to the 3-D swim is improved of some corrective (resistive and axial) forces which are neglected in the L.A.E.B.T. The resulting model is exploited in 5 and 6 respectively devoted to the external dynamics and the fast numerical algorithm. The next section (7) deals with the Navier-Stokes simulation in subsection 7.1, which is finally used in 7.3 and 7.4 for the calibration and validation of the analytical model. Lastly, the article ends with section 8 by some concluding remarks and perspectives.

2 Modeling of the body

In [40] we proposed to model an hyper-redundant robot as a nonlinear Cosserat beam internally actuated through a torque distribution (cf. figure 3). By "Cosserat-beam" we here mean a one-dimensional continuum obtained by the continuous assemblage of an infinity of cross sections of infinitesimal thickness. As it is stipulated in [41], the configuration space ($\mathcal{C}$) of such a medium is defined by the functional space of curves in the Lie group $SE(3)$:

$$\mathcal{C} = \{g(.) : X_1 \in [0,1] \mapsto g(X_1) \in SE(3)\}, \tag{1}$$

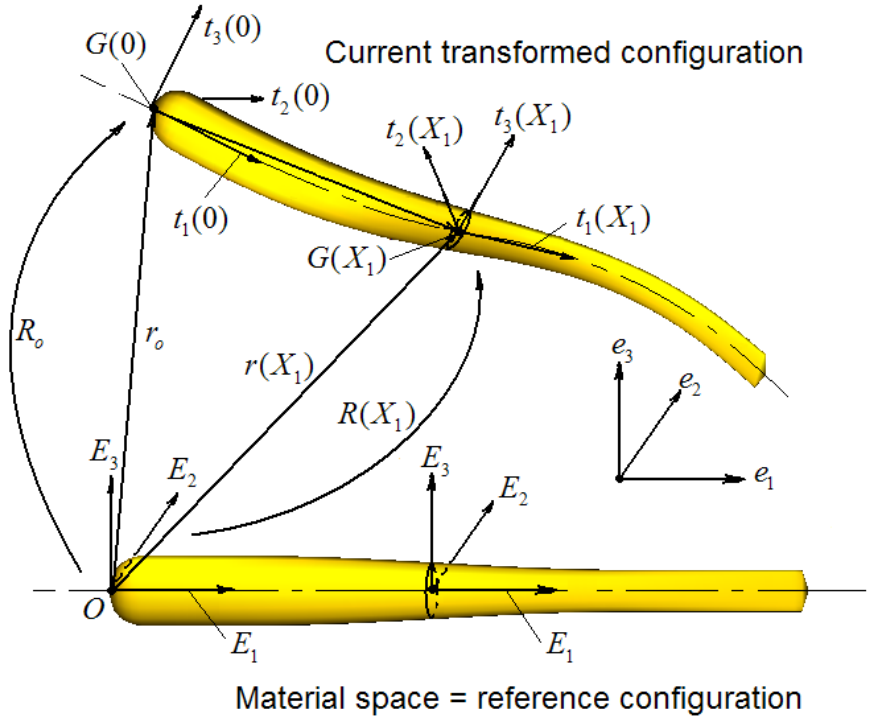

FIG. 3 – General notations of body kinematics.

where X_1 is the material abscissa along the beam axis and where any $g(X_1)$ is represented by the homogeneous transformation :

$$g(X_1) = \begin{pmatrix} R(X_1) & r(X_1) \\ 0 & 1 \end{pmatrix}, \tag{2}$$

with $R(X_1)$ and $r(X_1)$ the rotation and position operators which map the material frame (O, E_1, E_2, E_3) of figure 3 onto the current mobile frame $(G, t_1, t_2, t_3)(X_1, t)$ attached to the X_1 cross section of mass center $G(X_1)$. Corollary to these definitions, we introduce the two following fields of (spatial) twist from $]0, 1[$ to $se(3)$ (here identified to $\mathbb{R}^6$).

- The twist field of velocities :

$$\mu = \frac{\partial g}{\partial t}.g^{-1} = \begin{pmatrix} \omega \\ v \end{pmatrix} = \sum_{i=1}^{i=3} \begin{pmatrix} \Omega_i t_i \\ V_i t_i \end{pmatrix}. \tag{3}$$

- The twist field of strains :

$$\chi = \frac{\partial g}{\partial X_1}.g^{-1} = \begin{pmatrix} k \\ \gamma \end{pmatrix} = \sum_{i=1}^{i=3} \begin{pmatrix} K_i t_i \\ \Gamma_i t_i \end{pmatrix}, \tag{4}$$

where ω and v (respectively k and γ) are the spatial angular and linear Galilean velocities (respectively, the spatial "curvature-twist" and "tangent" vectors) along the beam. This framework named "macro-continuous" in [40] is particularly well suited to the modeling of hyper-redundant robots inspired from snake, trunk and other eels... In fact, in this case the beam axis models the animal back-bone while its cross-sections stand for its vertebrae. Going further, if the robot, as in the case here considered, is designed as a serial assemblage of parallel platforms, the Cosserat beam model is nothing but a continuous asymptotic limit of the hybrid (serial/parallel)

dynamic model [42], where the cross sections play the role of the rigid platforms of the multi-body robot and X_1 this of a continuous index. Moreover, the internal beam kinematics (Kirchhoff, Timoshenko...) are merely an infinitesimal version of the robot parallel kinematics. For instance, in the case here considered, the parallel kinematics introduce between each pair of contiguous platforms a universal joint where the pitch and yaw degrees of freedom are actuated (cf. figure 2). Thus the beam kinematics are those of non-twistable and non-extensible Kirchhoff beams, a model where the following internal kinematic constraints are forced :

$$\chi = \begin{pmatrix} k \\ \gamma \end{pmatrix} = \begin{pmatrix} k_d(t) \\ t_1 \end{pmatrix} = \chi_d(t), \tag{5}$$

with $k_d(t) = K_{d,2}(t)t_2 + K_{d,3}(t)t_3$, the field of internal curvature imposed along the beam by the internal control torque law. Finally, with these choices, the Lagrangian of the body $\mathcal{B}$ can be defined as $L(\mathcal{B}) = T(\mathcal{B}) - U(\mathcal{B})$ where :

- $T(\mathcal{B})$ is the kinetic energy of the body defined by :

$$T(\mathcal{B}) = \int_0^1 \mathfrak{T}_b \, dX_1 = \frac{1}{2} \int_0^1 \mu.\mathbb{I}_b.\mu \, dX_1, \tag{6}$$

with $\mathfrak{T}_b$ and $\mathbb{I}_b$ the densities (per unit of beam length) of kinetic energy and of inertia tensor, where the second is defined by :

$$\mathbb{I}_b = \begin{pmatrix} I_b & 0 \\ 0 & m_b \end{pmatrix}. \tag{7}$$

In (7) m_b and I_b are the linear and angular inertia tensor densities which can be detailed as : $m_b = \rho_b A \sum_{i=1}^{i=3} t_i \otimes t_i$, $I_b = \rho_b \sum_{i=1}^{i=3} J_i t_i \otimes t_i$, with ρ_b the beam volume mass, and A, J_i the cross section area and inertia about t_i, $i = 1, 2, 3$.

- $U(\mathcal{B})$ is the internal body potential energy defined by :

$$U(\mathcal{B}) = \int_0^1 \mathfrak{U}_b \, dX_1 = \int_0^1 \lambda.(\chi - \chi_d) \, dX_1. \tag{8}$$

Lastly, the following densities of wrenches of kinetic amounts and internal forces are introduced :

$$\begin{pmatrix} \sigma_b \\ p_b \end{pmatrix} = \frac{\partial \mathfrak{T}_b}{\partial \mu} = \begin{pmatrix} I_b.\omega \\ m_b.v \end{pmatrix} \ , \ \begin{pmatrix} c \\ n \end{pmatrix} = \lambda = \frac{\partial \mathfrak{U}_b}{\partial \chi}, \tag{9}$$

where σ_b, p_b, c, n are respectively the density fields of kinetic momentum, kinetic resultant, internal torque and internal force, with : $c.t_\alpha = C_\alpha, \alpha = 2, 3$, the two (pitching and yawing) control torque laws.

3 Dynamic modeling of the anguilliform swim

In this section, we reconsider the three dynamic modeling problems pointed out in the introduction and give to each of them a solution suited to the on-line control.

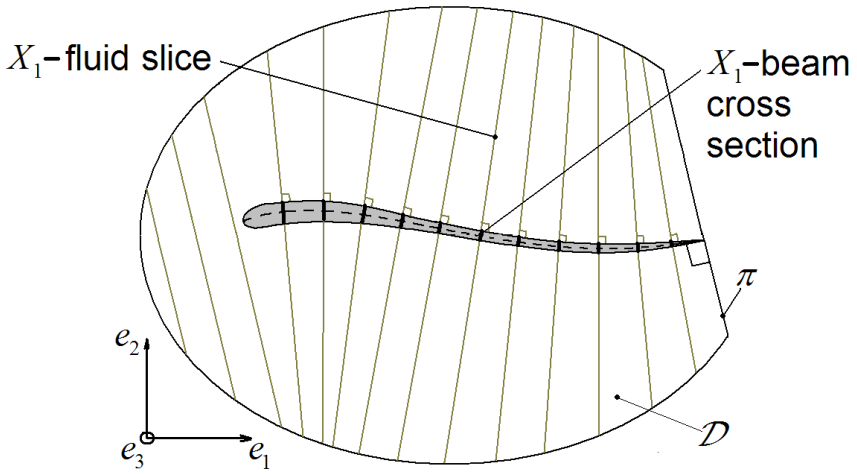

FIG. 4 – Stratification of the flow in $\mathcal{D}$.

3.1 Modeling the contact of the robot with the medium

In order to achieve our starting goals, the modeling efforts have to be particularly concentrated onto the "fluid-fish" contact model. In fact, the Navier-Stokes equations are very difficult to solve and completely unsuited to robotics. Hence, in order to circumvent this difficulty we should simplify as much as possible the fluid dynamics while keeping an acceptable accuracy regarding the robustness of the feedback control law [43]. Coming back to the original ideas of James Lighthill (see [22]), the contact model here proposed is based on the following two great simplifications :

• First simplification : The fluid is first of all considered as inviscid, incompressible and is irrotational everywhere except on a free vortex sheet shedded from the sharp trailing edge of the caudal fin. Still following Lighthill, the wake is then isolated from the flow laterally surrounding the fish by a geometric plane π orthogonal to the fish backbone and passing through the trailing edge. Hence, only the fluid contained in the control volume $\mathcal{D}$ of figure 4 is considered and the effects of the wake onto the fish are modeled through the kinetic exchanges with the fluid in $\mathcal{D}$ across the plane π.

• Second simplification : Due to the slender geometry of the fish (and the robot), and in accordance with the L.A.E.B.T., the fluid flow in $\mathcal{D}$ is approximated by a stratification of planar potential flows transverse to the fish back-bone. Hence, in this theory, the original three-dimensional fluid is replaced by a one-dimensional medium where the fluid slices (sweeping past the beam cross sections) replace the usual punctual fluid particles of the the 3-D theory (cf. figure 4).

Finally, this stratification allows one to write the kinetic energy of the fluid contained in $\mathcal{D}$ (denoted by $\mathcal{F}_\mathcal{D}$), under the following reduced form :

$$T(\mathcal{F}_\mathcal{D}) = \int_0^1 \mathfrak{T}_f \, dX_1 = \frac{1}{2} \int_0^1 \mu.\mathbb{I}_f.\mu \, dX_1, \tag{10}$$

where $\mathfrak{T}_f$ denotes the density (per unit of beam length) of kinetic energy of the stratified fluid in $\mathcal{D}$ and $\mathbb{I}_f$ is this of fluid added mass inertia which can be detailed as :

$$\mathbb{I}_f = \begin{pmatrix} I_f & 0 \\ 0 & m_f \end{pmatrix}, \tag{11}$$

where I_f and m_f are the density field of linear and angular fluid added inertia defined as : $I_f = \rho_f J_{f1} t_1 \otimes t_1$ and $m_f = \rho_f \sum_{2=1}^{i=3} A_{fi} t_i \otimes t_i$, ρ_f is the fluid volume mass, and A_{fi} (respectively J_{f1}) the added cross section area (respectively, inertia) along $t_i, i = 2, 3$, (respectively about t_1). Once this kinetic energy density is defined, the ideal fluid dynamics [44], allow one to introduce the following wrench density of impulses (a concept historically due to Lord Kelvin) :

$$\begin{pmatrix} \sigma_f \\ p_f \end{pmatrix} = \frac{\partial \mathfrak{T}_f}{\partial \mu} = \begin{pmatrix} I_f.\omega \\ m_f.v \end{pmatrix}, \tag{12}$$

which is merely an extension to the three-dimensional swim of the density of lateral impulses introduced by James Lighthill in his "Large Amplitude Elongated Body Theory" of [25]. Finally, in accordance with the Kirchhoff theory of solid bodies moving in an irrotational ideal fluid [35], the fluid dynamics in $\mathcal{D}$ are now reduced onto the configuration space of the beam alone. Furthermore all the effects of the fluid onto the body are modeled through added inertia which will be reported onto the external and internal dynamics, which is the only subject of our attention in the following.

3.2 Internal dynamics

The internal dynamics of the eel-like robot are given by the partial differential equations (p.d.e.'s) of the actuated Cosserat beam immersed in the fluid. In order to derive these equations we stated in [1] the following variational principle related to all the fluid and body matter contained in the mobile volume control $\mathcal{D}$:

$$\begin{aligned} &\int_{t_1}^{t_2} \left(\int_0^1 \delta(\mathfrak{T}_f + \mathfrak{T}_b - \mathfrak{U}_b)\ dX_1 \right) dt \\ &= \int_{t_1}^{t_2} \left(\delta W_{ext} - \left[\left(V_1 \frac{\partial \mathfrak{T}_f}{\partial \mu} - \mathfrak{T}_f \begin{pmatrix} 0 \\ t_1 \end{pmatrix} \right) .\delta\nu \right]_0^1 \right) dt, \end{aligned} \tag{13}$$

where the terms in brackets model the kinetic exchanges of the fluid in $\mathcal{D}$, with its wake (V_1 is merely the axial velocity of the stratified fluid with respect to the beam) while δW_{ext} stands for the virtual work of some corrective forces that we will add later and which are neglected by the L.A.E.B.T.. In their generality, these forces are defined as a field of wrench density $\overline{f}^T = (\overline{c}^T, \overline{n}^T)$ on $]0, 1[$ and two punctual wrenches $f_-^T = (c_-^T, n_-^T)$ and $f_+^T = (c_+^T, n_+^T)$ exerted onto the first and the last beam cross sections respectively. Finally, applying (13) for any variation $\delta\nu = \delta g.g^{-1}$ defined on the beam configuration space (1), one finds :

- Field equations :

$$\begin{aligned} &\frac{\partial}{\partial t} \begin{pmatrix} \sigma_b + \sigma_f \\ p_b + p_f \end{pmatrix} + \begin{pmatrix} v \times p_f \\ 0 \end{pmatrix} = \begin{pmatrix} \overline{c} \\ \overline{n} \end{pmatrix} + \\ &\frac{\partial}{\partial X_1} \begin{pmatrix} c + V_1 \sigma_f \\ n + V_1 p_f \end{pmatrix} + \begin{pmatrix} t_1 \times (n + V_1 p_f) \\ 0 \end{pmatrix}. \end{aligned} \tag{14}$$

• Boundary conditions :

$$\begin{pmatrix} c \\ n \end{pmatrix}(0) = \begin{pmatrix} 0 \\ -\mathfrak{T}_f t_1 \end{pmatrix}(0) + \begin{pmatrix} c_- \\ n_- \end{pmatrix}, \tag{15}$$

$$\begin{pmatrix} c \\ n \end{pmatrix}(1) = \begin{pmatrix} 0 \\ -\mathfrak{T}_f t_1 \end{pmatrix}(1) - \begin{pmatrix} c_+ \\ n_+ \end{pmatrix}. \tag{16}$$

Furthermore, by replacing in these equations the kinetic amounts by their expressions as functions of the beam kinematics and by using the change of variable : $n_* = n + V_1 m_f.v$ and $c_* = c + V_1 I_f.\omega$, (14-16) can be rewritten as :

• P.d.e. and boundary conditions (b.c.) of the internal forces :

$$n_*' = m.\dot{v} + \omega \times (m_f.v) - m_f.(\omega \times v) + \overline{n}, \tag{17}$$

$$n_*(0) = n_-, \quad n_*(1) = (V_1 m_f.v - \mathfrak{T}_f t_1)(1). \tag{18}$$

• P.d.e. and b.c. of the internal torques :

$$c_*' = -t_1 \times n_* + I.\dot{\omega} + \omega \times I.\omega + v \times m_f.v + \overline{c}, \tag{19}$$

$$c_*(0) = 0 \ , \ c_*(1) = (V_1 I_f.\omega)(1), \tag{20}$$

where from now on, $\partial./\partial X_1$ and $\partial./\partial t$ are respectively denoted by a "prime" and a "dot", and where, because of the rounded nose, we take $\mathbb{I}_f(0) = 0$.

4 Resistive corrections of the (reactive) 3-D Lighthill model

In this section, we add to the previous "reactive model" and through the term δW_{ext} of the balance (13), there are two sets of corrections. The first one has for its purpose to improve the L.A.E.B.T. around the rounded nose where the axial forces, neglected by the S.B.T. (see [32]), dominate. The second set of corrections approximates the effect of the fluid viscosity. As far as the first correction is concerned, it depends on geometric shape of the head which here is the half of an ellipsoid where the axis lengths are $2c_o$, $2a_o$ and $2b_o$ along $t_1(0)$, $t_2(0)$ and $t_3(0)$ respectively. On the other hand, the second correction is based on the experimental fluid mechanics of cylindrical obstacles moving in a real fluid [45]. Like buoyancy and gravity, all these corrections are added to the reactive model through the general external load $(\overline{n}, \overline{c}, n_\pm, c_\pm)$. In fact we first impose that the two tip external wrenches be of the following form :

$$\begin{pmatrix} c_- \\ n_- \end{pmatrix} = \begin{pmatrix} c_{r-} \\ n_{r-} \end{pmatrix} + \begin{pmatrix} c_{a-} \\ n_{a-} \end{pmatrix} \ , \ \begin{pmatrix} c_+ \\ n_+ \end{pmatrix} = 0 \ , \tag{21}$$

with :

$$\begin{pmatrix} c_{r-} \\ n_{r-} \end{pmatrix} = -\frac{1}{2}\rho_f k_o \begin{pmatrix} 0 \\ V_1|V_1|t_1 \end{pmatrix}(0), \tag{22}$$

and $k_o = \pi c_p a_o b_o$, the axial "pressure drag" coefficient of the rounded nose. As far as the second term of (21.a) is concerned, we take :

$$\begin{pmatrix} c_{a-} \\ n_{a-} \end{pmatrix} = -m_o \begin{pmatrix} 0 \\ (t_1.\dot{v})t_1 \end{pmatrix}(0), \tag{23}$$

where $m_o = \rho_f \pi k a_o b_o c_o$ models the added mass axially accelerated with the rounded nose of the eel. Then, following a Taylor-like resistive modeling approach, the second set of corrections is imposed through the following density of external resistive wrenches :

$$\begin{pmatrix} \overline{c}_r \\ \overline{n}_r \end{pmatrix} = -\frac{1}{2}\rho_f \begin{pmatrix} k_4|\Omega_1|\Omega_1 t_1 \\ \sum_{i=1}^{i=3} k_i V_i |V_i| t_i \end{pmatrix}, \tag{24}$$

where from experimental fluid mechanics : $k_4 = c_1\pi(a^2 - b^2)^2$; $k_1 = c_f P$ (with $P \simeq \pi/2((3/2)(a+b) - \sqrt{ab})$ standing for the elliptic cross section perimeter), $k_2 = c_2 2a$ and $k_3 = c_3 2b$. Finally, this last corrective wrench density has to be added to the gravity and buoyancy densities in such a manner that we finally have, with γ_g the gravity acceleration field :

$$\begin{pmatrix} \overline{c} \\ \overline{n} \end{pmatrix} = \begin{pmatrix} \overline{c}_r \\ \overline{n}_r \end{pmatrix} + \begin{pmatrix} 0 \\ (\rho_b - \rho_f) A \gamma_g \end{pmatrix}. \tag{25}$$

Lastly, in accordance to experimental fluid mechanics [45], the corrections (22), (23) and (24) use the following dimension-less coefficients. The coefficients c_p and k are the "axial pressure drag" and the axial added mass coefficient of the head, while for the X_1-elliptic cross section, $c_f(X_1)$, $c_1(X_1)$, $c_2(X_1)$ and $c_3(X_1)$ are respectively the friction coefficient, the angular drag coefficient (around $t_1(X_1)$), and the two linear drag coefficients along $t_2(X_1)$ and $t_3(X_1)$.

5 External dynamics

From now on, we use the following notations : $r(X_1 = 0) = r_o$, $R(0) = R_o$, $g_o = g(0)$, $\mu_o = (\dot{g}.g^{-1})(0)$ for the head frame configuration and twist. Furthermore, we introduce the co-adjoint maps Ad_{g*} and Ad^*_g respectively defined for any g given by (2) as :

$$Ad_{g*} = \begin{pmatrix} 1 & 0 \\ -\widehat{r} & 1 \end{pmatrix}, \; Ad^*_g = \begin{pmatrix} 1 & \widehat{r} \\ 0 & 1 \end{pmatrix} \tag{26}$$

The external dynamics rule the time-evolution of the external degrees of freedom here parameterized by the head configuration $g_o \in SE(3)$. This evolution being driven by the explicit time dependent curvature law, the external dynamics can be derived by restating the internal dynamics (14-16) in the weak form of the D'Alembert principle, where the virtual displacement fields are induced by those of the head frame while the body shape is frozen in its current configuration. Finally, with $h(X_1) = g_o^{-1}.g(X_1)$, $p = p_b + p_f$ and $\sigma = \sigma_b + \sigma_f$, we have :

$$\begin{aligned} \int_0^1 Ad^*_h \begin{pmatrix} \dot{\sigma} - \overline{c} \\ \dot{p} - \overline{n} \end{pmatrix} + \begin{pmatrix} v \times p_f \\ 0 \end{pmatrix} dX_1 = \begin{pmatrix} c_- \\ n_- \end{pmatrix} \\ + \quad Ad^*_{h(1)} \left(V_1 \begin{pmatrix} \sigma_f \\ p_f \end{pmatrix} - \begin{pmatrix} 0 \\ \mathfrak{T}_f t_1 \end{pmatrix} \right)(1). \end{aligned} \tag{27}$$

Then, for numerical purposes, these dynamics have to be rewritten as an explicit form of the head accelerations. For this, $\dot{p}$ and $\dot{\sigma}$ have to be explicitly rewritten in terms of the beam Galilean accelerations $\dot{\omega}$ and $\dot{v}$ which themselves have to be rewritten as :

$$\begin{pmatrix} \dot{\omega} \\ \dot{v} \end{pmatrix} = Ad_{h*}. \begin{pmatrix} \dot{\omega}_o \\ \dot{v}_o \end{pmatrix} + \begin{pmatrix} \dot{\omega}_e \\ \gamma_e \end{pmatrix}, \tag{28}$$

which defines $\dot{\omega}_e$ and γ_e since $\mu_o = (\omega_o^T, v_o^T)^T$ is the spatial twist of the head frame velocities. Finally, thanks to (28), we can rewrite (27) from simple but tedious computations as the explicit o.d.e. with respect to the head accelerations :

$$\mathbb{I}_o.\dot{\mu}_o = \mathbb{F}_o, \tag{29}$$

where we introduced, if "$\mathbb{I} = \mathbb{I}_b + \mathbb{I}_f$" defines the total (body + fluid) density of inertia along the robot, the 6×6 spatial inertia tensor of solid and added masses w.r.t. the nose :

$$\mathbb{I}_o = \int_0^1 Ad_h^*.\ \mathbb{I}\ .Ad_{h*}\ dX_1 + \begin{pmatrix} 0 & 0 \\ 0 & m_o(t_1 \otimes t_1)(0) \end{pmatrix}, \tag{30}$$

$$\begin{aligned} \text{and :} \qquad \mathbb{F}_o = & \int_0^1 \mathbb{I}. \begin{pmatrix} \dot{\omega}_e \\ \gamma_e \end{pmatrix} dX_1 + \begin{pmatrix} c_{r-} \\ n_{r-} \end{pmatrix} + \\ & \int_0^1 Ad_h^*. \begin{pmatrix} \omega \times I.\omega + (v \times m_f.v) + \overline{c} \\ \omega \times m_f.v - m_f.(\omega \times v) + \overline{n} \end{pmatrix} dX_1 \\ + \quad & Ad_{h(1)}^* \left(V_1 \begin{pmatrix} \sigma_f \\ p_f \end{pmatrix} - \begin{pmatrix} 0 \\ \mathfrak{T}_f t_1 \end{pmatrix} \right)(1), \end{aligned} \tag{31}$$

the wrench of inertial (Coriolis-centrifugal, convective...) and external (hydrodynamic, hydrostatic...) forces applied onto the fish head.

6 Fast algorithm

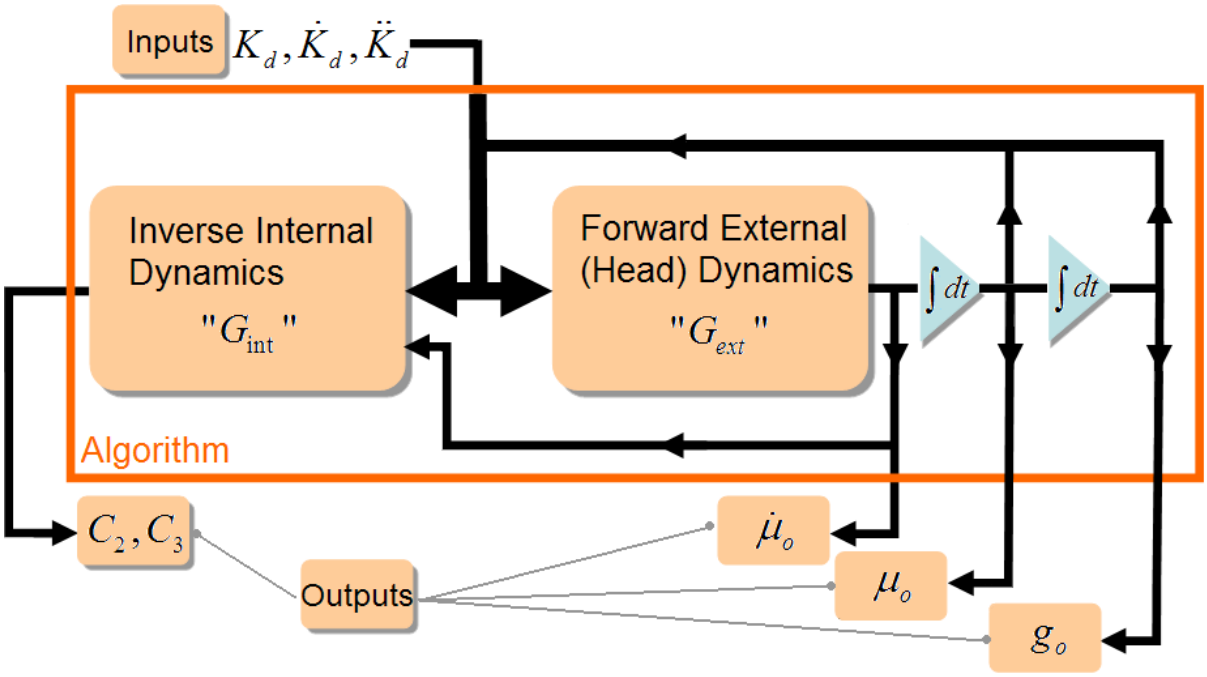

FIG. 5 – Macro-continuous fast algorithm.

For the purposes of simulation, design and control it is useful to compute at each instant the head acceleration $\dot{\mu}_o$ and the internal control torque law $C = R^T.(c - (c.t_1)t_1) = C_2E_2 + C_3E_3$

from the knowledge of the material internal curvature law $K_d(t) = R^T.k_d(t) = K_{d,2}(t)E_2 + K_{d,3}(t)E_3$. To this purpose, we proposed in [40] an algorithm (see its structure in figure 5) which solves at each step of a global time integration loop :

- The forward (external) dynamics :

$$\dot{\mu}_o = G_{ext}(g_o, \mu_o, K_d(t), \dot{K}_d(t), \ddot{K}_d(t)) \tag{32}$$

- The inverse (internal) dynamics :

$$C = G_{int}(g_o, \mu_o, \dot{\mu}_o, K_d(t), \dot{K}_d(t), \ddot{K}_d(t)). \tag{33}$$

Because computing explicitly G_{ext} and G_{int} is very involved, we compute them numerically using the implicit formulation of the Newton-Euler Robot dynamics (see [46, 47, 48], for more details) where the actuated beam is considered as a continuous robot and the usual recurrences on the bodies index of the Newton-Euler algorithms are replaced by some o.d.e.'s with respect to the cross section label X_1. Such a computation is based on (17,19), (29,30,31) and the following continuous kinematics derived from (4) and (5) and their time differential consequences [40] :

- Continuous model of section transformations

$$R' = R.\widehat{K}_d(t) \ , \ r' = R.E_1. \tag{34}$$

- Continuous model of section velocities :

$$\omega' = R.\dot{K}_d(t) \ , \ v' = \omega \times r'. \tag{35}$$

- Continuous model of section accelerations :

$$\dot{\omega}' = R.\ddot{K}_d(t) + \omega \times R.\dot{K}_d(t) \ , \ \dot{v}' = \dot{\omega} \times r' + \omega \times (\omega \times r'). \tag{36}$$

Now, we have at our disposal all the results required for solving the two G_{int} and G_{ext} dynamics. In fact, let us assume that at the current time t of a global time-loop, we know the current head state $(g_o, \mu_o)(t)$, then :

- For computing G_{ext}, the algorithm forward space integrates (i.e. from $X_1 = 0$ to $X_1 = 1$), (34) with $g(0) = g_o$, (35) with $\mu(0) = \mu_o$, and (36) with $\dot{\mu}(0) = 0$. These integrations give respectively the fields (R, r), (ω, v) and $(\gamma_e, \dot{\omega}_e)$. Then, from (30) and (31), both computed by a similar forward space integration, we finally obtain through the explicit form (29) the head acceleration $\dot{\mu}_o$ that is time-integrated twice in order to update the head state (g_o, μ_o) (see figure 5).

- For computing G_{int}, and because now $\dot{\mu}_o$ is known, the algorithm computes through a forward space integration of (36) with $\dot{\mu}(0) = \dot{\mu}_o$, the Galilean acceleration fields $\dot{\omega}$ and $\dot{v}$ along the beam. Then, once these fields are known, it computes the field n^* by forward space integrating (17), and from n^*, it integrates (19) in order to compute c^* and $c = c^* - V_1 I_f.\omega$. Finally, the control torque law is deduced from : $C_2 = c.t_2$ and $C_3 = c.t_3$.

Lastly, once G_{ext} and G_{int} so computed, the time is increased by one step and the algorithm resumes...

7 Simulations and comparisons

7.1 Navier-Stokes computational approach

In order to validate the simplified model presented in this article, we chose to use reference data coming from the resolution of the same fluid-structure problem but solving the 3-D Navier-Stokes equations. This complex problem of a self-propelled three-dimensional fish on realistic configurations (high Reynolds number and possible complex geometry) recently received a solution in the context of the ISIS-CFD software package developed by some of the partners of our project ([13, 14]). In fact, most of the numerical results of fish locomotion immersed in a viscous flow do not concern "self-propelled" bodies but rather bodies undergoing some imposed deformations superimposed on a given stationary overall rigid motion or equivalently, a steady past-flow (see [12]). Nevertheless, [11] proposed a 2-D Navier-Stokes simulator of a self-propelled deformable body but restricted their investigations to the straightforward swim for very simplified planar body shapes. [15] also performed some 2-D self-propelled simulations by imposing internal control torques along the body. Using quite similar methods, the only other 3-D simulations we found in the literature were performed with a low Reynolds number range (around 3000) and then under a laminar flow hypothesis (see [16]).

Given the size and the speed of our robot (leading to Reynolds number of about 6.10^5 for the presented results), this hypothesis of laminar flow is not realistic here. In fact, when Reynolds number increases, the viscous stresses are overcome by the fluid inertial forces, and the laminar motion becomes unstable. Rapid random velocity and pressure fluctuations appear : turbulence occurs. The enormous amount of information and the huge grid density required to completely describe such a turbulent flow on realistic configurations (like those presented here) is totally out of reach of current computer power yet. An average procedure (introduced by Reynolds in 1895) of the instantaneous Navier-Stokes equations is then still needed to investigate turbulent flows. This statistical approach consists in expressing all quantities as the sum of mean and fluctuating parts. The so-called Reynolds Average Navier-Stokes (RANS) equations obtained are identical to the instantaneous ones with mean velocity and pressure replacing instantaneous quantities, except a supply fluctuating correlation term $\tau_t(i,j) = -\rho\overline{\widetilde{u}_i\widetilde{u}_j}$, which appears in the momentum balance (see (37)), and is referred to the Reynolds stress tensor ($\widetilde{u}_i$ means the fluctuation of the component i of the velocity and the overline represents the average process). Indeed, the whole complexity of turbulent flows is contained in this term, which needs to be modeled to close the system of equations. It is classically evaluated using additional transport equations of supply variables (turbulent kinetic energy,...).

Hence, the incompressible turbulent flow of newtonian viscous fluid under isothermal conditions are solved through the following classical RANS equations (respectively momentum balance, incompressibility constraint and newtonian fluid behavior law) :

$$\rho_f\left(\frac{\partial\overline{u}}{\partial t} + \nabla\overline{u}.\overline{u}\right) = -\nabla\overline{p} + \rho_f\gamma_g + \nabla.(\overline{\tau}_t + \tau_t), \tag{37}$$

$$\nabla.\overline{u} = 0, \tag{38}$$

$$\overline{\tau} = \mu_f\left(\nabla\overline{u} + (\nabla\overline{u})^T\right), \tag{39}$$

where ρ_f and μ_f are respectively, the density and the molecular dynamic viscosity of the fluid, γ_g is the gravity acceleration field, $(\overline{u}, \overline{p})$ represent the average values of velocity and pressure (through the Reynolds processing), while $\overline{\tau}$ and $\overline{\tau_t}$ refer respectively to the viscous and Reynolds stress tensors. Finally, $\overline{\tau}$ follows the classical relation of Newtonian fluid for incompressible flows (39), while τ_t is determined according to the turbulence model used, through supply equations

which are not presented here (for further details on turbulence modeling, see for example [49] or [50]).

ISIS-CFD is a CFD software for simulating incompressible fluid flows involving turbulence, free surface and moving bodies ([51, 52, 53]). It has been developed by the CFD team of the Fluid Dynamics Laboratory of Ecole Centrale de Nantes. It solves the incompressible unsteady RANS equations under isothermal conditions on generalized unstructured meshes, enabling to deal with geometries of arbitrary complexity. The solver is based on a face-based finite-volume method to build the spatial discretization of the equations previously described. Second-order accurate schemes in time and in space are used. Because the case deals with a moving body, an ALE (Arbitrary Lagrangian Eulerian) approach is used : an additional equation (the so-called space conservation law) has to be taken into account, too. In ISIS-CFD, this geometric constraint is directly addressed through the evaluation of the grid velocity fluxes, which ensures that the discrete space conservation equation is exactly satisfied (see [13, 54]).

As far as the body dynamics are concerned, the Navier-Stokes solver only deals with the external dynamics which are here derived from a floating frame approach (until now, ISIS-CFD has been restricted to the planar swim, but development is planned to perform at short term 3-D swim). Originally devoted to flexible spacecraft dynamics [55], this description measures the deformations of the body with respect to a virtual rigid body $\mathcal{B}_*$ to which is attached the floating frame and which follows the real one ($\mathcal{B}$) in its motion.

In the case here studied, the floating frame is placed at the mass center of $\mathcal{B}_*$ itself defined as the rigid geometry prolonging $\mathcal{B}$ from the head at each instant t. Then, if $g_* \in SE(3)$ denotes the floating frame configuration with respect to the earth, the time-evolution of its Galilean twist $\dot{g}_*.g_*^{-1} = \mu_*$ is ruled by the following balance of wrenches (related to G_*) :

$$\mathbb{I}_*.\dot{\mu}_* = \mathbb{F}_{in*} + \mathbb{F}_{hyd*} \quad , \tag{40}$$

where we introduced $\mathbb{I}_*$ the inertia tensor of the actual body, $\mathbb{F}_{in,*}$ the wrench of inertia forces (due to Coriolis, centrifugal and shape accelerations of the body), and $\mathbb{F}_{hyd*}$ the wrench of hydrodynamic forces given by integrating all the contact forces exerted by the fluid onto the body boundaries and computed through the resolution of (37). For more details about these expressions, we refer the reader to [13]. It is worth noting that an internal mesh for solved motion of flexible body is required to compute additional dynamic terms induced by the imposed deformation. On the other hand, the body kinematics influence the flow via the boundary conditions on fluid induced on each body face.

Thus, the resolution of the flow/motion coupling at each time step progresses as shown in the diagram figure 6.

Concerning the deformation part of the fluid domain invoked at the beginning of each time step to keep a body-fitted mesh, an analytical weighted regridding, taking advantage of the Cosserat kinematics of the body, has been developed [14]. During the non-linear iterations inside a given time step, the mesh (and so the current position of the body) is moved and updated in space by the rigid solved transformation h_* without any deformation, enabling fish motion of unlimitated amplitudes (see figure 7).

The computational grid used here has been limited to its upper part ($x_3 \geq 0$), with a symmetry condition on the plane $x_3 = 0$ (see figure 8). A grid independence study has been investigated to ensure the numerical error is under control. Therefore, several mesh have been generated, with different grid density (from 65000 to 900000 cells). The influence of the turbulence model has also been investigated. Examining all these simulations performed on the $F1$ imposed law (see (42)-(44) and tab. 1), differences between all the reached forward velocities do not exceed 5 %, whatever the grid and the turbulence model used (the influence of the turbulence modelling being then of the same order of magnitude as differences obtained with all the tested

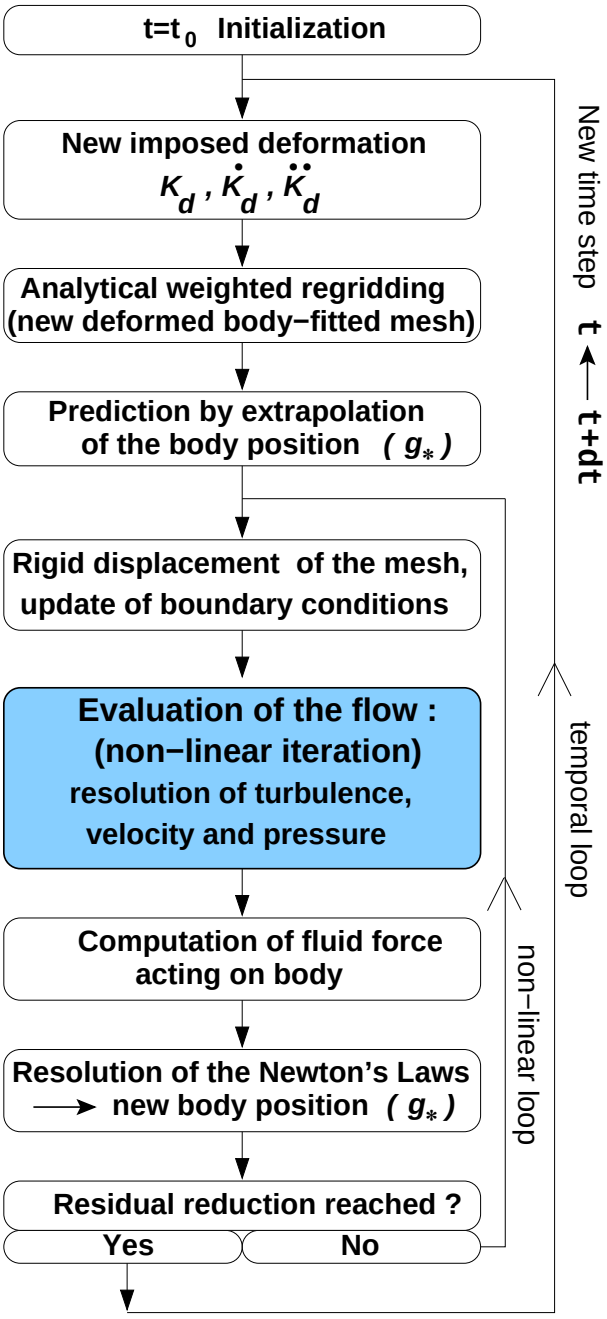

FIG. 6 – Flow/motion coupling algorithm of the Navier-Stokes solver.

grids). Keeping in mind that the main objective is to validate the dynamics of a simplified model, all the comparisons with the simplified model were performed on the coarser mesh containing 65.10^3 cells using the $k-\omega$ SST turbulence model [13]. It ensures reasonable CPU time, a good compromise between accuracy and CPU time cost, and enables comparisons with the simplified model to be confidently tackled.

More details of all numerical aspects and validations concerning the resolution of the RANS equations and the flow/motion coupling can be found in [13] and in [14].

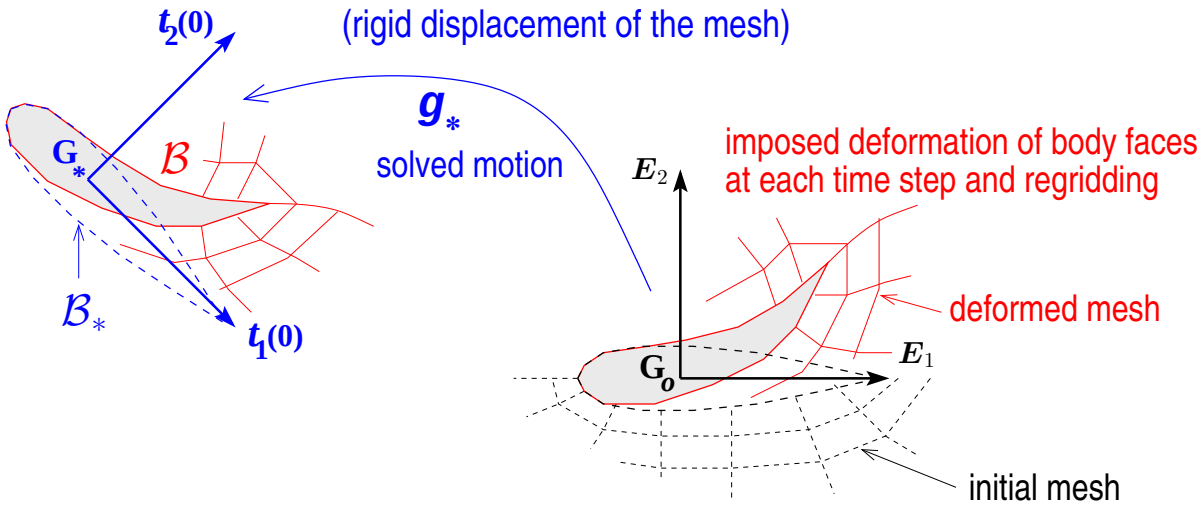

FIG. 7 – Regridding strategy : deformation/motion splitting for the Navier-Stokes solver.

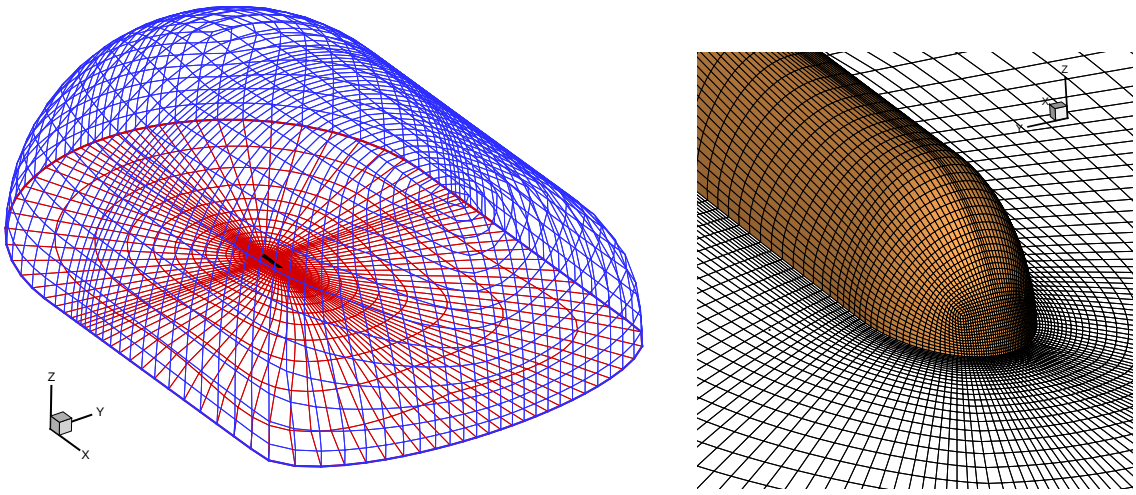

(a) Global view of mesh.

(b) Mesh around the head of the robot.

FIG. 8 – Mesh structured of 65.10^3 elements.

7.2 Definition of the body geometry

In order to take into account the continuous property of the skin, we consider the previous macroscopic modeling with the geometry drawn in the figure 9. Its total length is one meter. Its material is assumed to be homogeneous with a "mass/volume" ratio equal to that of the fluid to ensure a buoyancy neutrality. Its mass is then of $1.94kg$. The shape is first defined as a cylinder of diameter $D = 0.1m$ between $X_1 = 0.05m$ and $X_1 = 0.99m$ ending by two half-ellipsoids. Next, this cylinder is deformed by multiplying its diameter along E_3 by a function $X_1 \mapsto A(X_1)$, and along E_2 by $X_1 \mapsto B(X_1)$. Therefore, elliptic cross sections are obtained. The two functions A and B are defined as follow :

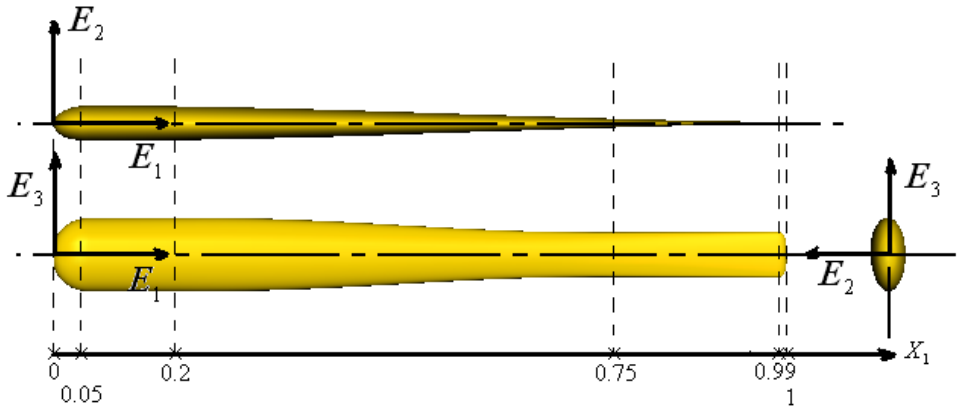

FIG. 9 – Geometry of the body.

$$\begin{aligned} A(X_1) &= 1 \text{ , for : } 0 \leq X_1 < 1/5, \\ A(\tilde{X_1}) &= 1 - (\sin(\pi \tilde{X_1} - \pi/2) + 1)/5 \text{ ,} \\ &\quad \text{for : } 1/5 \leq X_1 < 3/4 \text{ ,} \\ &\quad \text{with } \tilde{X_1} = 20X_1 - 4/11, \\ A(X_1) &= 3/5 \text{ , for : } 3/4 \leq X_1 < 1, \end{aligned}$$

and for $0 \leq X_1 < 1$:

$$B(X_1) = -\left[\sin\left(\pi X_1 - \pi/2\right) + 1\right]/6 - X_1^2/8 + 1/2 \text{ .}$$

Note in particular, that such a geometry guarantees to the head to be a half ellipsoid with axis lengths $b_0 = 0.025m$, $a_0 = c_0 = 0.05m$ respectively along t_2, t_1 and t_3.

7.3 Calibration of the model

In accordance with the previous developments, we have to specify the four groups of parameters of the model, i.e. : the axial viscous drag coefficient c_f of (24), the pressure drag coefficient c_p related to the rounded nose of the head required by (22), the transverse pressure drag coefficients c_1, c_2 and c_3 of (24), the axial added mass of the nose m_o required by (23).

In order to fix all these parameters, we used the following "identification process" divided into four steps :

• Step 1 : identification of c_f

To estimate the local viscous drag coefficient c_f along the body, a model based only on classical relations of boundary layer on a flat plate (which only depends on the local longitudinal Reynolds number) was established. Even if this simple approach completely ignores the shape and the deformation of the body, it can hopefully approximate the right order of magnitude of the longitudinal viscous drag force. Since the RANS simulations do not yet take into account correctly the transition phenomena, a study of the behavior of the turbulence model used here was performed. Hence, flow around a 2-D thin flat plate in a unbounded domain was simulated using the $k - \omega$ SST turbulence model in its near-wall low Re configuration. The plot of the

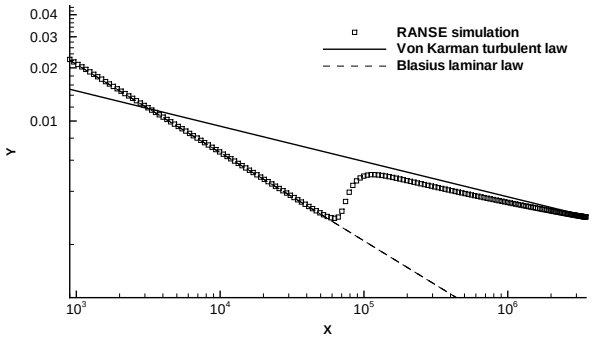

FIG. 10 – Extraction of the local friction coefficient on a 2-D thin plate where X=$Re_{X_1//}$ and $Y = c_f$.

values of c_f as a function of the local axial Reynolds number $Re_{X_1//}$ (see figure 10) shows that the model leaves the laminar Blasius curve towards the turbulent Von Karman curve at about $Re_{X_1//} = 8.10^4$.

The law for the local viscous drag coefficient was then chosen as :

$$\begin{aligned} &\text{if } Re_{X_1//} \leq 8.10^4 \text{ , } c_f = 0.664/Re_{X_1//}^{0.5}, \\ &\text{if } Re_{X_1//} > 8.10^4 \text{ , } c_f = 0.059/Re_{X_1//}^{1/5}, \end{aligned} \tag{41}$$

where $Re_{X_1//}$ is defined by : $Re_{X_1//} = X_1 V_1(X_1)/\nu$, with ν the kinematic viscosity of water.

• Step 2 : identification of c_p

The coefficient c_p is identified by comparing the Navier-Stokes simulations to those of the simplified model for a gait in which the fish is released with an initial forward speed in a straight and rigid configuration. In this case, the fish slows down by enduring the c_p dependent pressure drag force of (22) applied onto the head, and the friction (viscous drag) axial forces of (24) applied along its body, with c_f known from the previous step. The plots of figure 11(a) show the evolution of the axial forward velocity for Navier-Stokes simulation and for the model (with c_p equal to 0 and the calibrated value 0.036). The plots of figure 11(b) show the two contributions to the total axial drag forces applied onto the fish (also plotted on the figure), i.e. the head force (22), and the body one (24). Note that the contribution due to the pressure applied onto the head represents about 16% of the total drag.

• Step 3 : identification of c_1, c_2 and c_3 :

As far as c_2 and c_3 are concerned, their values should be time dependent through the transverse Reynolds numbers and the Keulegan-Carpenter numbers [56], which qualify the flow around an oscillating cylinder. Nevertheless, the problem here is quite different to experiments that can be found in the literature on oscillating cylinders. In fact, due to the forward fish motion, the flow perturbations generated by a given cross-section no longer influence the section itself but rather the neighboring sections along the beam axis. Furthermore, the amplitude of oscillations changes when moving along the body, and finally, the sections do not have circular profiles but elliptic ones for which fewer experimental results are available. Nevertheless, in spite of these difficulties, some simple models were successfully used. Particularly, in accordance with the experimental data : 1°) of [45] for different 2-D shapes plunged in a stationary flow (for our orders of magnitude of the transverse Reynolds $Re_{X_1\perp} \simeq 10^4$), and : 2°) of [57], for a normal flat plate, the constant value of 1.98 was chosen for c_2. From similar considerations, c_3 was set to the lower

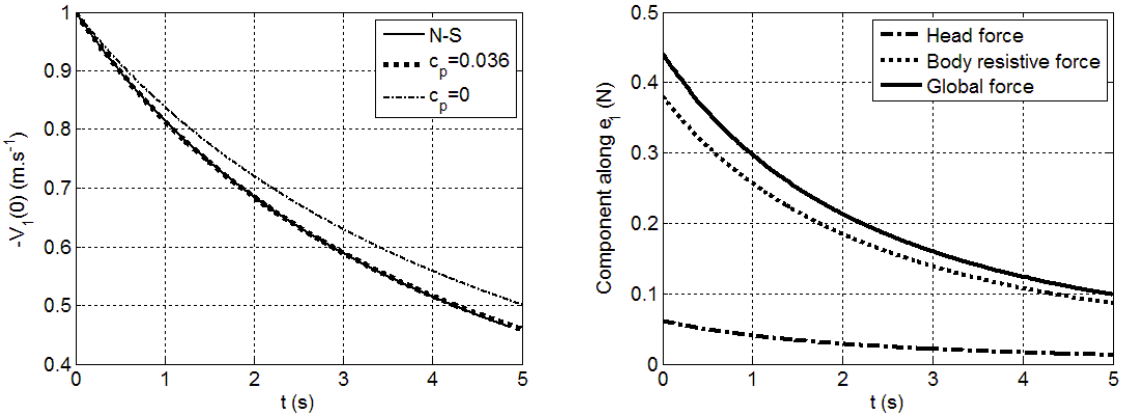

(a) Identification of c_p. (b) Drag forces on the eel.

FIG. 11 – Step 2 : identification of c_p, with c_f fixed by step 1.

value of 0.5, in order to take into account the thinner cross section profile along this direction. As far as the resistive torque density $\bar{c}_r$ is concerned, since the Navier-Stokes solver does not work for the three dimensional swim, we cannot yet shape a relevant analytical form of it. So we took $c_1 = 0$ as a first value. Finally note that in the following, c_1 and c_3 are only concerned by the last numerical test, which is the only one dealing with a three dimensional manoeuvre.

• Step 4 : identification of k

With the adopted geometry of the head, we chose to take for m_o, the half axial added mass of an ellipsoid enduring a translation along its principal major axis. The dimensionless coefficient k computed by [44] is equal to 0.32.

Finally, as we are going to see, this setting of the analytical model was confirmed in many examples by comparison to our RANS equations solver.

7.4 Numerical examples

The fast algorithm of section 6 was programmed in C++ using a fourth order Runge-Kutta integrator for the space and time loops. All the tests presented above work between "0.2 and 0.7 times the real time" on a workstation with a Pentium IV (3.2 GHz and 1 Go of Ram) and are therefore compatible with the online control of the prototype. As announced from the beginning, the swim of the body is imposed through the field of desired curvatures $X_1 \mapsto k_d(X_1, t) = R(X_1).K_d(X_1)$ imposed along the body axis. Here, we simulate four swimming gaits : the "forward straight-line gaits" denoted by $F.$, the "planar turn gait", denoted by $T.$, the "stopping gait" denoted by $S.t.$, and finally the "three dimensional spiral gaits", denoted by $S.p.$. Moreover, this is achieved with several sets of parameters for $F.$ and $T.$ and for three ways of turning. In the case of the planar swim, the results given by our simplified analytical model are compared to Navier-Stokes simulations.

7.4.1 Example 1 : forward nominal gait

Definition of the internal strain law : this gait is that of the nominal "straight-line swim" as commonly studied in zoological literature [3, 58, 59, 60]. In our case, the swim being achieved in the plane (e_1, e_2), it is defined by the following curvature law (with "f " for "forward") :

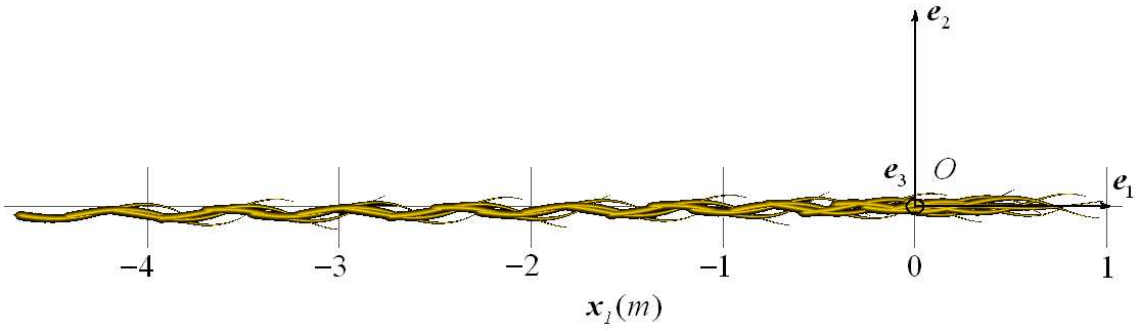

FIG. 12 – The body's trajectory for the forward gait $F1$ ($1fps$).

Gaits	λ	T	a_2	a_1	a_0	ϕ	V_{init}
$F1$	1	1	2	0.5	1	0	0
$F2$	1.25	1	2	1	0	0	0
$F3$	1	0.5	2	0.5	1	0	-0.6
$F4$	1	1.5	2	0.5	1	0	-0.6
$F5$	1	1	1	0.5	2	0	-0.6
$F6$	0.75	1	1	0.5	2	0	-0.6
$F7$	1	1	3.5	-4.5	2	0	-0.6

TAB. 1 – Parameters of the forward straight-line gaits (44).

$$k_d = f_r(t, 0, T) K_{f3}(t, X_1) t_3(X_1), \tag{42}$$

where $f_r(t, t_i, t_f)$ is a sinusoid ramp defined by (with $\tau = (t - t_i)/(t_f - t_i)$) :

$$\begin{aligned} f_r &= 0 \text{ , for : } 0 \leq t < t_i, \\ f_r &= \tau - 1/(2\pi) \sin(2\pi\tau) \text{ , for : } t_i \leq t < t_f, \\ f_r &= 1 \text{ , for : } t \geq t_f. \end{aligned} \tag{43}$$

Note here that $f_r(., t_i, t_f)$ has null first and second order derivatives at the commutation instants thereby guaranteeing time-smooth starts. The non-null curvature component is a backward sinusoidal wave from the head to the tail which can be detailed as :

$$\begin{aligned} &K_{f3} = f_a(X_1) \sin\left[2\pi \left(X_1/\lambda - t/T + \phi\right)\right] \text{ ,} \\ &\text{with } f_a(X_1) = a_2 X_1^2 + a_1 X_1 + a_0 \text{ .} \end{aligned} \tag{44}$$

In (44), λ is the wave length, T is its period and a_0, a_1, a_2 are the coefficients of the amplitude modulation polynomial function f_a which increases from the head to the tail. ϕ is a possible phase shift (used only for the turning gaits). Because (42) leads to a steady periodical motion ("cruising swim"), the fish, initially straight along e_1, can be threw with an initial forward velocity ($\dot{r}_o(t_i) \triangleq V_{init} t_1(0)$, where t_i is the initial time of simulation), in order to shorten the time of execution of the Navier-Stokes simulations.

Numerical results : for this example, we applied the strain law (42)-(44) with the parameters of the table 1. The results obtained with our simplified model were then compared with those

Gaits	$\overline{V}_{1,N-S}(0)$ $(m.s^{-1})$	$\overline{V}_{1,S-M}(0)$ $(m.s^{-1})$	$e_{\overline{V}_1}$ (%)
$F1$	0.642	0.619	1.9
$F2$	0.613	0.614	0.2
$F3$	1.310	1.270	3.1
$F4$	0.412	0.407	1.2
$F5$	0.753	0.721	4.2
$F6$	0.452	0.456	0.9
$F7$	0.278	0.306	9

TAB. 2 – Comparisons N-S/S-M for forward gaits.

given by the Navier-Stokes reference used under the same conditions. In order to quantify the comparison, we used the following error ratio related to the average axial head velocity in the steady periodic motion :

$$e_{\overline{V}_1} = \frac{|\overline{V}_{1,N-S}(0) - \overline{V}_{1,S-M}(0)|}{|\overline{V}_{1,N-S}(0)|},$$

where "$N-S$" means "Navier-Stokes", "$S-M$" means "Simplified-Model", and $\overline{V}_1(0) = \overline{V}_1(X_1 = 0)$ is the mean axial head velocity reached at any time beyond which the fish follows its steady periodical motion. The error ratios for the parameters of the table 1 are summarized in the table 2.

As an illustration, the figures 13(a), 13(b) and 13(c) show the time evolutions of the head velocity obtained for $F1$ with the Navier-Stokes solver and the simplified-model-based-algorithm of the article. The components of the velocities are related to the earth frame. All the components oscillate with the propulsion period of K_{f3} and the plots show good agreement (in phases and amplitude) of the simplified model with the Navier-Stokes reference (even for the transverse and yawing velocities of small amplitudes). Finally, all these plots like others tested with (42)-(44) and many sets of parameters show the right accordance (less than 5% of discrepancies) of the simplified model when compared to the reference, except for $F7$ where the difference is due to the low steady velocity reached by the fish (see table 2). In fact, when the Reynolds decreases, the model of c_f becomes less and less suited and particularly more dependent on the fish deformations.

7.4.2 Example 2 : Turning gaits

Definition of the internal strain law. This gait is deduced from the previous one by adding to the propulsive curvature term of (42), a constant planar curvature K_{c3} along the body. More precisely, we take :

$$k_d(t) = (\alpha(t)K_{f3} + \beta(t)K_{c3})\, t_3, \tag{45}$$

where $\alpha(.)$ and $\beta(.)$ are two transition functions which allow a smooth starting and a smooth suppression and re-installation of the propulsion at the beginning and the end of the turn.

Numerical results : in this test, the internal law (45) is applied to three types of turns. The first type denoted "$T.i.p.$", is an inertial-turn with a propulsion before and after the turning phase Φ_2 (laws $T1$, $T2$ and $T3$ plotted on figure 14 left), the second type, denoted "$T.p.$", is a propulsive turn (the robot does not stop to undulate while turning) (law T4 plotted on figure 14

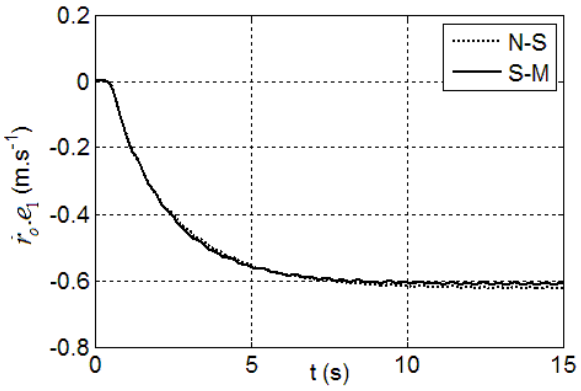

(a) Linear head velocity along e_1.

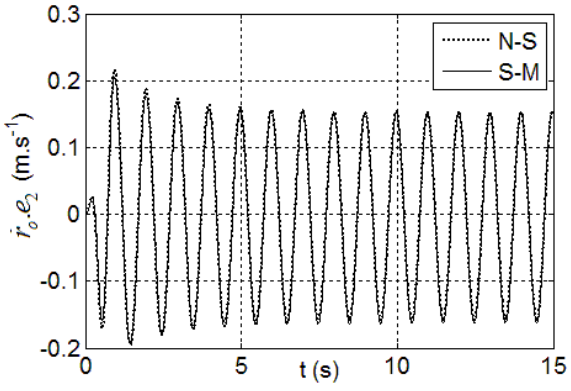

(b) Linear head velocity along e_2.

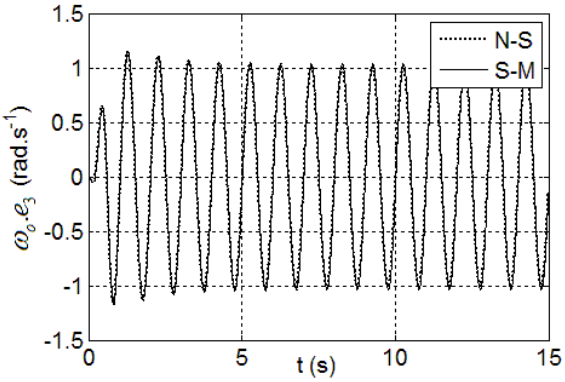

(c) Angular head velocity along e_3.

FIG. 13 – Comparisons between N-S/S-M for $F1$ forward gait.

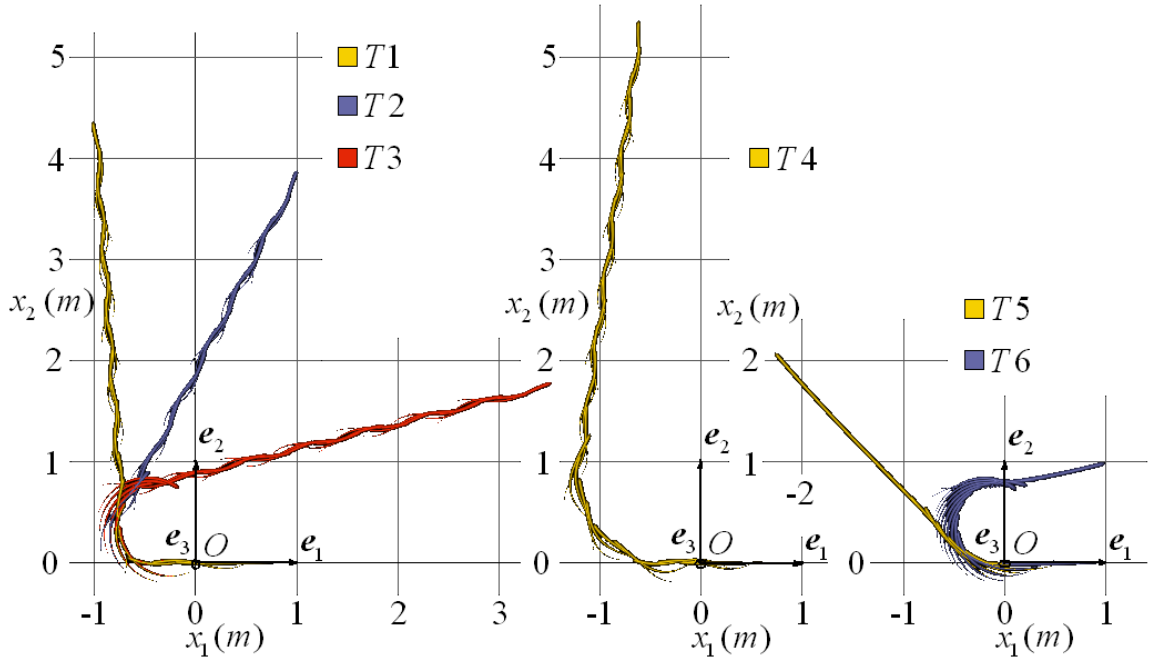

FIG. 14 – Visualization of all the turning gaits ($1f/0.4s$).

Gaits	$T1$	$T2$	$T3$	$T4$	$T5$	$T6$
type	$T.i.p.$	$T.i.p.$	$T.i.p.$	$T.p.$	$T.i.$	$T.i.$
λ	1	1	1	1	-	-
T	1	1	1	1	-	-
a_2	2	2	2	2	-	-
a_1	0.5	0.5	0.5	0.5	-	-
a_0	1	1	1	1	-	-
ϕ	1/4	1/4	1/4	1/4	-	-
V_{init}	-0.6	-0.6	-0.6	-0.6	-0.6	-0.6
K_{c3}	2	2	2	1	1	2
t_1	1.5	1.5	1.5	1.5	0.25	0.25
t_2	2	2.5	3.5	3.5	0.75	1.25
t_3	2.5	3	4	4	1.75	4.25
t_4	-	-	-	-	2.25	5.25

TAB. 3 – Parameters of the turning gaits.

center). Finally, the third type, denoted "$T.i.$", corresponds to a pure inertial turn with just an initial axial velocity and no self propulsion (laws $T5$ and $T6$, plotted on figure 14 right). These three types of turning gait are defined as follow :

- T.i.p. gait :

$$\begin{aligned} \alpha(t) = f_r(t,0,T)\ ,\ \beta(t) = 0 \quad &, \text{for :} \quad t < T, \\ \alpha(t) = 1 - \beta(t) = 1 - f_r(t,T,t_1) \quad &, \text{for :} \quad T \leq t < t_2, \\ \alpha(t) = 1 - \beta(t) = f_r(t,t_2,t_3) \quad &, \text{for :} \quad t \geq t_2. \end{aligned}$$

- T.p. gait :

$$\begin{aligned} \alpha(t) = f_r(t,0,T)\ ,\ \beta(t) = 0 \quad &, \text{for :} \quad t < T, \\ \alpha(t) = 1\ ,\ \beta(t) = f_r(t,T,t_1) \quad &, \text{for :} \quad T \leq t < t_2, \\ \alpha(t) = 1\ ,\ \beta(t) = 1 - f_r(t,t_2,t_3) \quad &, \text{for :} \quad t \geq t_2. \end{aligned}$$

- T.i. gait :

$$\begin{aligned} \alpha(t) = 0\ ,\ \beta(t) = 0 \quad &, \text{for :} \quad t < t_1, \\ \alpha(t) = 0\ ,\ \beta(t) = f_r(t,t_1,t_2) \quad &, \text{for :} \quad t_1 \leq t < t_3, \\ \alpha(t) = 0\ ,\ \beta(t) = 1 - f_r(t,t_3,t_4) \quad &, \text{for :} \quad t \geq t_3. \end{aligned}$$

The simulations were experimented with the parameters given in the table 3.

In the case of the turn, we compared the yaw angle of the head at any time beyond which the fish has reached its steady periodical motion after the turn. The yaw angle ψ is that of the head axis $t_1(X_1 = 0)$ with respect to e_1, and we denote by $\overline{\psi}$, its mean value computed at any time beyond the turn is ended and the steady motion reached. Due to this definition, we can construct the following yaw error ratio :

$$e_{\overline{\psi}} = \frac{|\overline{\psi}_{N-S} - \overline{\psi}_{S-M}|}{|\overline{\psi}_{N-S}|},$$

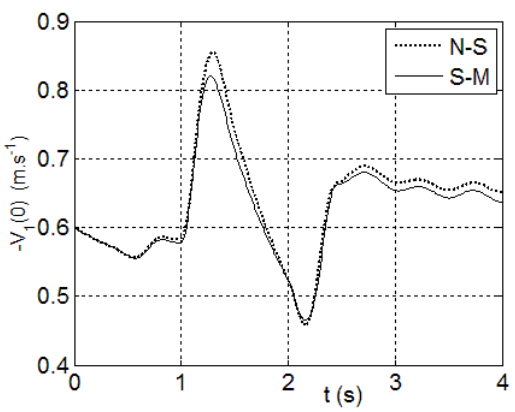

(a) Forward head velocity.

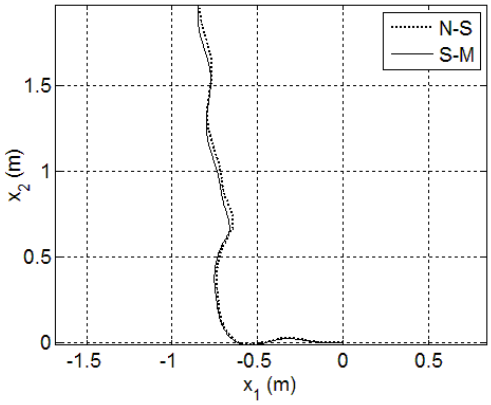

(b) Head trajectory.

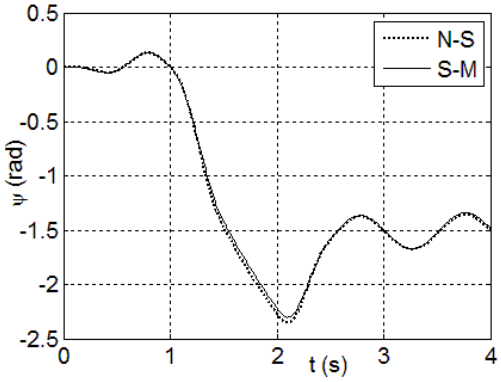

(c) Yaw head angle.

FIG. 15 – Comparisons between N-S/S-M for $T1$ turning gait.

which is used to compare the results of the Navier-Stokes ("N-S") simulator and those of the simplified model ("S-M"). These comparisons are summarized in table 4.

For all the turns we experimented, the error on the yaw does not exceed 10%, which is fully acceptable for any robust feedback control law of the swim as those proposed in [43]. For the purpose of illustration, we give on the figures 15(a)-(c) the time evolutions of the norm of the head velocity, its position vector in the swimming plane, and its yaw angle for the turn $T1$.

7.4.3 Example 3 : stopping gaits

This gait is obtained by imposing a forward undulation (from the tail to the head) still of the form (42) and (44) while the fish is moving forward (cf. figure 16). This is in accordance with the experimental observation of anguilliform fishes such as the European eel [60]. In nature the role of the body is assisted by that of the pectoral fins to stop the fish.

Numerical results : Taking (42), (44) with the parameters of table 5, while the fish has an initial axial velocity $\dot{r}_o = V_{init}(0)t_1(0)$, gives the results of figures 17(a)-(c) for both the simplified model and the Navier-Stokes based one. This stopping law does not appear to be very efficient when velocity becomes low. In the range of slow motion, amplitudes of deformation should be larger to obtain a clearer stopping. In the case of the animal, the pectoral fins may also be used

Gaits	$\overline{\psi}_{N-S}$ (deg)	$\overline{\psi}_{S-M}$ (deg)	$e_{\overline{\psi}}$ (%)
$T1$	-88	-86	1.96
$T2$	-116	-117	0.9
$T3$	-163	-166	1.75
$T4$	-94	-98	4.27
$T5$	-45	-49	8.09
$T6$	-157	-167	6.57

TAB. 4 – Comparison N-S/S-M for the turning gaits.

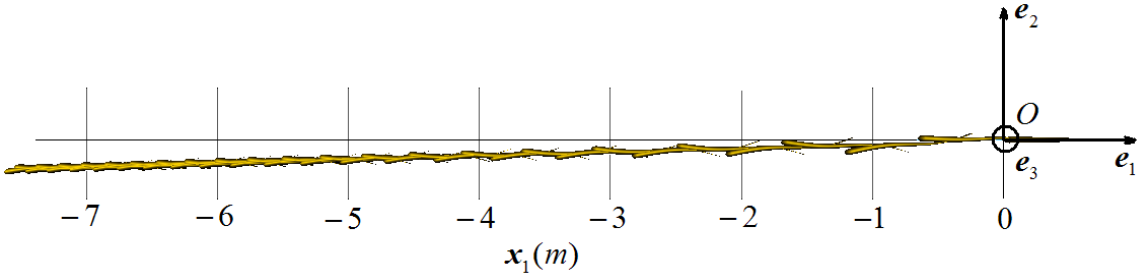

FIG. 16 – Stopping gait ($2fps$).

to actually (and efficiently) stop and maintain its body at rest. In this case, the following error ratio was used (where '0' here stands for "$X_1 = 0$") :

$$e_{\overline{V_1}} = \frac{|\overline{V}_{1,N-S}(0) - \overline{V}_{1,S-M}(0)|}{|V_{init}|}.$$

In these conditions, the values of velocities and error ratio at the final time of the simulation $t_f = 20s$ are given in table 6.

Finally, because the velocity tends to zero, the same remarks as those evoked for the forward gait $F7$ in the low Reynolds apply in this gait.

7.5 Three dimensional gait : the spiral manoeuvre or three-dimensional turn

Definition of the internal strain law : This gait consists of applying to the body two constant curvatures, plus a propulsive one normal to the plane of the swim.

$$k_d(t) = f_r(t, 0, T)(K_{f3}t_3 + K_{c2}t_2 + K_{c3}t_3), \tag{46}$$

where K_{c2} and K_{c3} are the constant pitch (along the field t_2) and yaw (along the field t_3) curvatures respectively, while K_{f3} is the "forward" yaw curvature of (44) still responsible of the undulating propulsion.

Gait	λ	T	a_2	a_1	a_0	V_{init}
Stopping	-1	1	0.5	0.5	0.5	-1.5

TAB. 5 – Parameters of the stopping gaits "S.T.I.".

Gait	$\overline{V}_{1,N-S}$ $(m.s^{-1})$	$\overline{V}_{1,S-M}$ $(m.s^{-1})$	$e_{\overline{V}_1}$ (%)
Stopping	0.0321	-0.0581	6

TAB. 6 – Comparison Simplified-Model/Navier-Stokes.

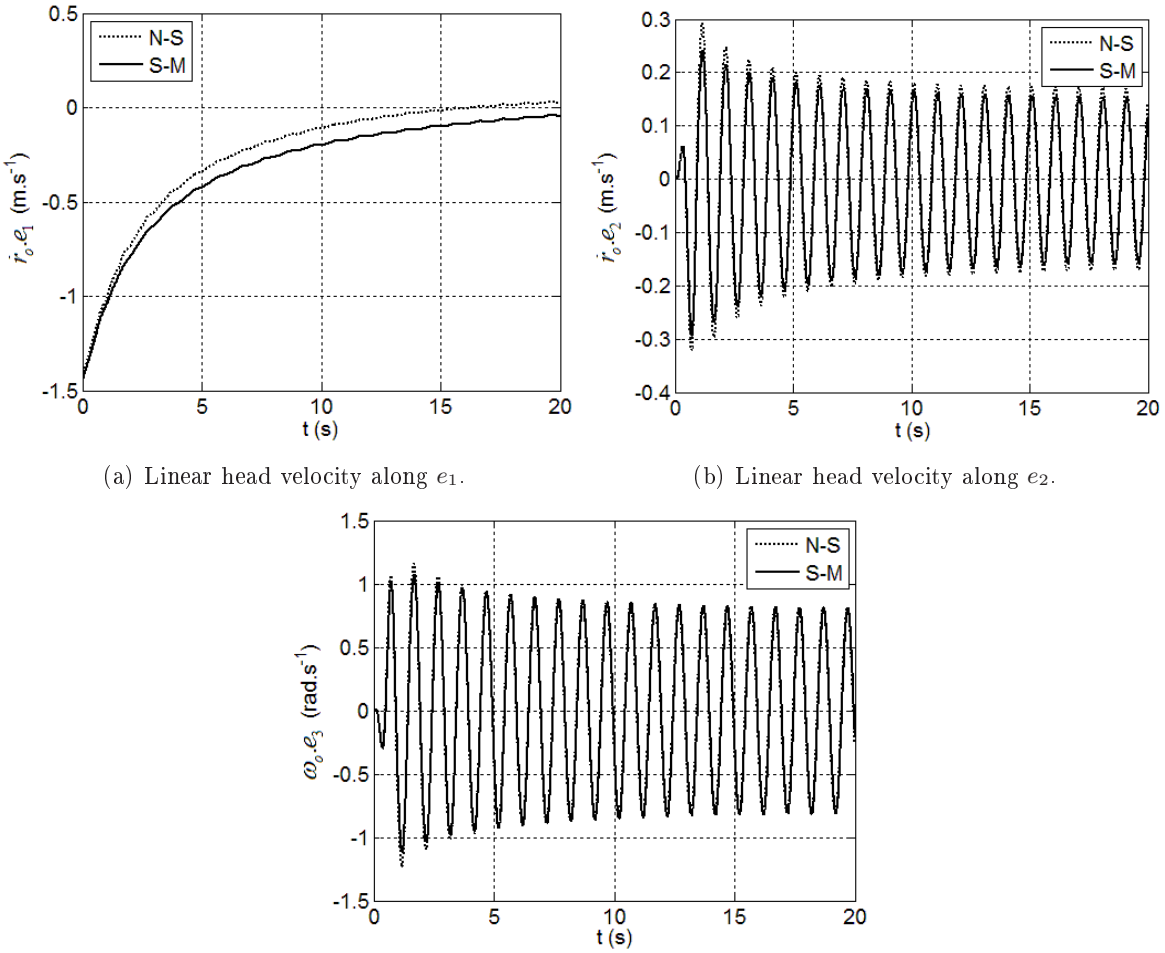

(a) Linear head velocity along e_1.

(b) Linear head velocity along e_2.

(c) Angular head velocity around e_3.

FIG. 17 – Comparisons between N-S/S-M for the stopping gait.

Numerical results : The test is obtained by applying (46), with the set of parameters given in the table 7. During the duration T, the body is curved in yaw and pitch. Thus, the fish maintains these curvatures along its body and rolls up along the spiral while propelling (figure 18). As far as the internal dynamics are concerned, figures 19(a)-(f) give the spatial distribution of the three components of the internal torque field $c_* = \sum_{i=1}^{i=3} C_{*i} t_i$ and the internal force field $n_* = \sum_{i=1}^{i=3} N_{*i} t_i$ evaluated all along the beam axis at the final time of the simulation. On the other hand, figures 20(a)-(f) validate the compatibility of the external dynamics with respect to the internal ones. In fact, the computation of the fields n_* and c_* at the tail boundary is achieved all along the time horizon (here of length $10s$) by forward space integrating (17) with the "initial condition" $n_*(0) = n_-$, and (19) with the "initial condition" $c_*(0) = 0$. In these conditions, we do obtain the final conditions : $n_*(1) = (V_1 m_f.v - \mathfrak{T}_f t_1)(1) = \sum_{i=1}^{i=3} N_{i,d} t_i$ and $c_*(1) = (V_1 I_f.\omega)(1) = \sum_{i=1}^{i=3} C_{i,d} t_i$ of (17) and (19), as required by the external dynamics.

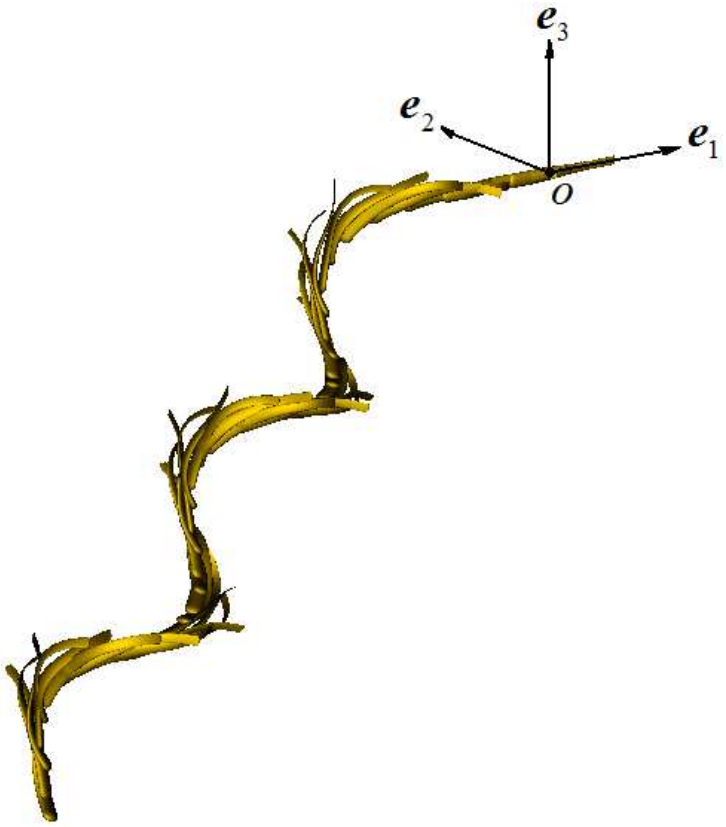

FIG. 18 – Three dimensional gait : the spiral (1f/1.5s).

Gait	λ	T	a_2	a_1	a_0	$\mathcal{V}_{init}$	K_{c2}	K_{c3}
Spiral	1	1	2	0.5	1	-0.6	1	1

TAB. 7 – Parameters of the spiral gait.

The figure 21 plots the axial and rolling velocities of the head. It is worth noting the non null (equal to 0.31 rad/sec.) average rolling velocity of the head which shows that the eel rolls around its backbone while plunging in a spiral. The high sensitivity of the roll dynamics to any perturbations (here generated by the couplings of the pitch and yaw dynamics and the boundary rolling terms) should require a detailed modeling of k_4 and the design of a specific stabilization controller using pectoral fins. Such a rolling-stabilizer will be included in the feedback controller of the whole 3-D motion of our future eel-like robot. Such feedback laws are today being designed and studied (with crude approximations of k_4) by our partners specialized in Automatic Control and are presented in [43]. Finally, the computations of the internal dynamics for all these tests (and others) were used in order to design the dimensions of our prototype and particularly those of the actuators (powers, maximal and nominal torques...).

8 Conclusion

In this article, a solution to the fast dynamics of eel-like robots has been proposed and tested. The solution works faster than the "real-time". It solves the problem of the numerical integration of the fish head dynamics while computing the control torque field required by the fish motions.

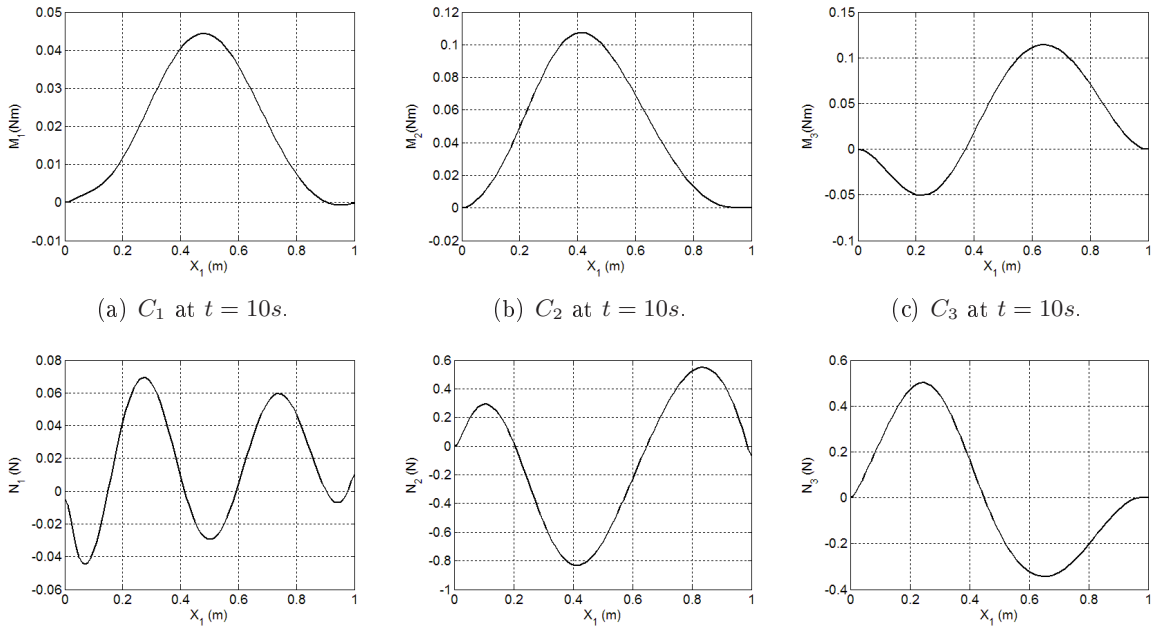

(a) C_1 at $t = 10s$. (b) C_2 at $t = 10s$. (c) C_3 at $t = 10s$.

(d) N_1 at $t = 10s$. (e) N_2 at $t = 10s$. (f) N_3 at $t = 10s$.

FIG. 19 – "X_1 profile" of components of the internal force (n) and torque (c) at $t = 10s$ for the spiral gait.

The proposed solution is based on a fast algorithm recently proposed in [40] for dealing with hyper-redundant robots dynamics and an extension of the Large Amplitude Elongated Body Theory of Lighthill to the three-dimensional self propelled swim [1]. From this initial framework a pure reactive model has been improved by some resistive corrective terms deduced from experimental fluid mechanics around obstacles and following a "trial and error tuning strategy" based on comparisons of the simplified model with a Navier-Stokes solver. It is worth noting here that, once this calibration achieved, the coefficients of the model were fixed definitively. Finally, the comparisons of our calibrated analytical model with the reference are very encouraging since they in fact do not exceed ten per cent for all the hight Reynolds planar cases tested until today. Nevertheless, the simplified model has now to be validated for the three dimensional swim for which our Navier-Stokes solver is not yet operational. Furthermore, the robot will be equipped in the future with lateral appendages that will mimic the pectoral fins of the fish and special attention will be paid to the roll dynamics which will be dealt with like a stabilization problem for the control feedback loops. The tail and the skin will also be designed and "optimized" with respect to the swimming efficiency under the constraints imposed by the actuators performances. This operation will be facilitated by the computation of the actuators power given by the internal dynamics presented in the article. Finally, based on a visual feedback, the remote-control of the prototype will be a first step towards autonomous navigation. Several experiments will be tested in swimming pools in order to qualify the bio-mimetic solution in terms of efficiency and manoeuvrability with respect to more conventional rigid underwater vehicles.

Acknowledgment

We would like to thank the French CNRS for supporting this work through the project "Robot Anguille" of the Interdisciplinary Research Program ROBEA. We acknowledge the constructive remarks of the reviewers, which have contributed to improve the quality of this paper.

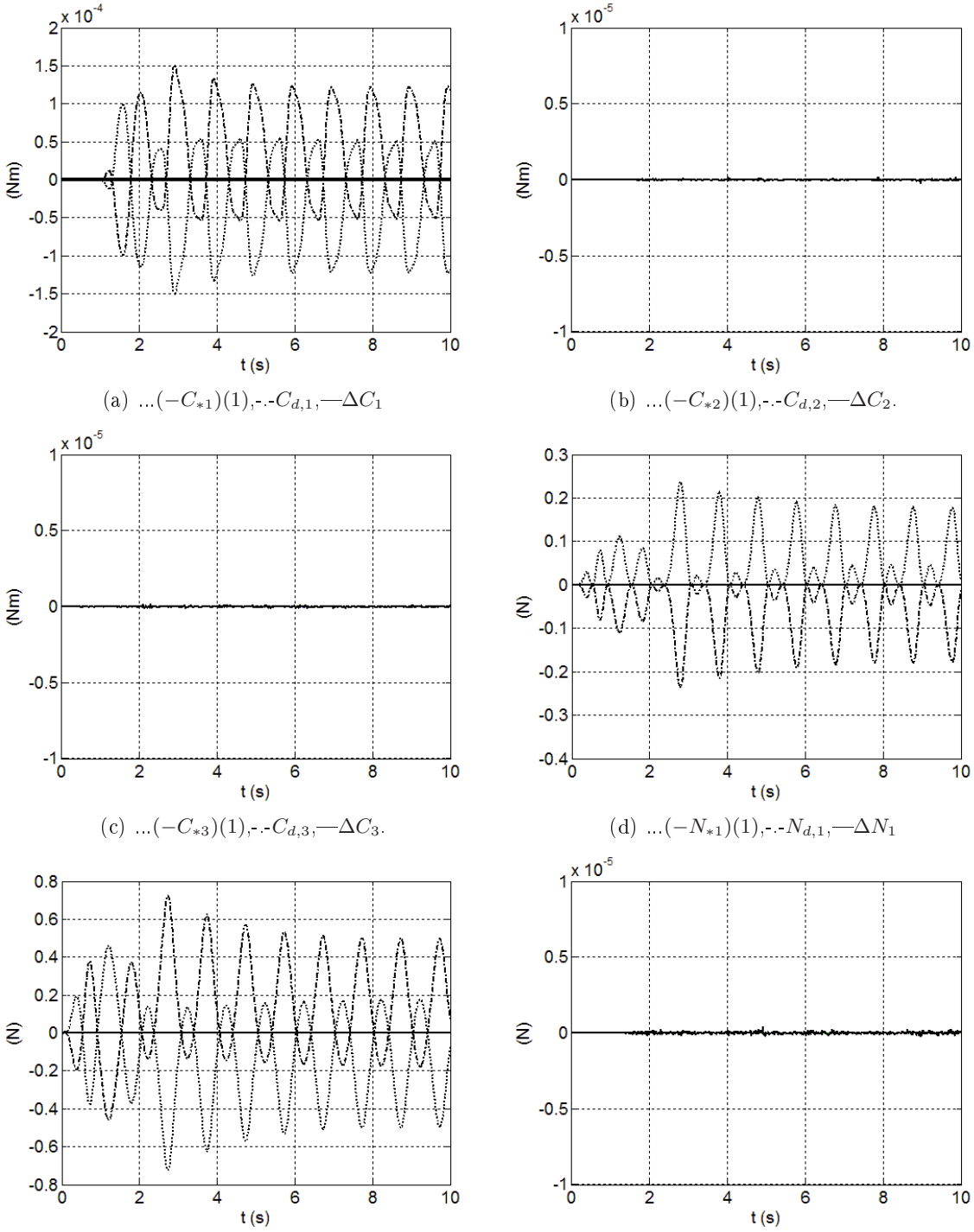

(a) ...$(-C_{*1})(1)$,-.-$C_{d,1}$,—ΔC_1

(b) ...$(-C_{*2})(1)$,-.-$C_{d,2}$,—ΔC_2.

(c) ...$(-C_{*3})(1)$,-.-$C_{d,3}$,—ΔC_3.

(d) ...$(-N_{*1})(1)$,-.-$N_{d,1}$,—ΔN_1

(e) ...$(-N_{*2})(1)$,-.-$N_{d,2}$,—ΔN_2.

(f) ...$(-N_{*3})(1)$,-.-$N_{d,3}$,—ΔN_3.

FIG. 20 – Time evolution of the boundary internal wrench $(c_*^T, n_*^T)^T(1)$ (its opposite) given by the forward space integration of (19,17), and $(c_d^T, n_d^T)^T$ directly given by (16), Δ. stands for their differences.

Références

[1] F. Boyer, M. Porez and A. Leroyer, "Poincaré-Cosserat equations for Lighthill three-dimensional dynamic model of a self propolled eel devoted to robotics", *Submitted, Technical*

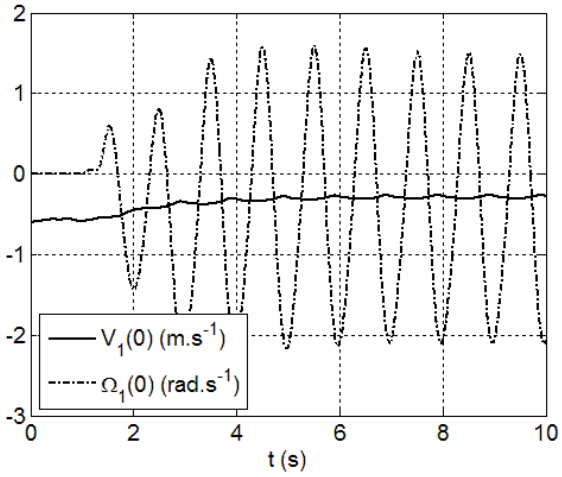

FIG. 21 – Time evolution of $V_1(0)$ and $\Omega_1(0)$.

Report of EMN and IRCCyN no. : 07/8/Auto [online]. Available : http ://www.irccyn.ec-nantes.fr/hebergement/Publications/2007/3721.pdf, 2007.

[2] K. A. McIsaac and J. P. Ostrowski, "A geometric approach to anguilliform locomotion modelling of an underwater eel robot", *IEEE Int. Conf. on Robotics and Automation*, Detroit, USA, 1999, vol.4, pp. 2843-2848.

[3] C. M. Breder, "The locomotion fishes", *Zoologica*, vol.4, pp. 159-256, 1926.

[4] R. Mason and J. W. Burdick, "Experiments in carangiform robotic fish locomotion", *IEEE Int. Conf. on Robotics and Automation*, San Francisco, USA, 2000, vol. 1, pp. 428-435.

[5] N. Kato, "Control performance in the horizontal plane of a fish robot with mechanical pectoral fins", *IEEE J. of Oceanic Engineering*, vol. 25, pp. 121-129, 2000.

[6] K. A. Morgansen, V. Duindam, R. J. Mason, J. W. Burdick and R. M. Murray, "Nonlinear control methods for planar carangiform robot fish locomotion", *IEEE Int. Conf. on Robotics and Automation*, Seoul, Korea, 2001, vol. 1 , pp. 427-434.

[7] J. Yu, M. Tan, S. Wang and E. Chen, "Development of a biomimetic robotic fsh and its control algorithm", *IEEE trans. on Systems, Man and Cybernetics - Part B : Cybernetics*, vol. 34, pp. 1798-1810, 2004.

[8] K. A. Morgansen, B. I. Triplett and D. J. Klein, "Geometric methods for modeling and control of free-actuated underwater vehicles", *Submitted to the IEEE Trans. on Robotics*, [online]. Available : http ://vger.aa.washington.edu/publications/tro-biorobotics-uwfish.pdf, 2007.

[9] J. P. Merlet, *Parallel robots*, Kluwer Academic Publishers, 2000.

[10] J. E. Colgate and K. M. Lynch, "Mechanics and control of swimming : a review", *IEEE J. of Oceanic Engineering*, 2004, vol. 29, pp. 660-673.

[11] J. Carling, T. L. Williams and G. Bowtell, "Self-propelled anguilliform swimming : simultaneous solution of the two-dimensional Navier-Stokes equations and Newton's laws of motion", *J. Experimental Biology*, vol. 201, pp. 3243-3166, 1998.

[12] Q. Liu and K. Kawachi, "A numerical study of undulatory swimming", *J. of Computational Physics*, vol. 155, pp. 223-247, 1999.

[13] A. Leroyer, "Flow/Motion interaction for solid and flexible bodies by resolution of the Navier-Stokes equations. Contribution to the numerical modelisation of cavitating flows",

Ph.D. dissertation, Ecole Centrale de Nantes et Université de Nantes, Nantes, France, December 2004.

[14] A. Leroyer and M. Visonneau, "Numerical methods for RANSE simulations of a self-propelled fish-like body", *J. of Fluids and Structures*, vol. 20, pp. 975-991, 2005.

[15] D. J. J. Farnell, T. David and D. C. Barton, "Numerical model of self-propulsion in a fluid", *J. of Royal Society Interface*, vol. 2, pp. 79-88, 2005.

[16] S. Kern and P. Koumoutsakos, "Simulations of optimized anguiliform swimming", *J. of Experimental Biology*, vol. 209, pp. 4841-4857, 2006.

[17] S. J. Hill, "Large amplitude fish swimming", Ph.D. dissertation, University of Leeds, September 1998.

[18] M. J. Wolfgang, "Hydrodynamics of flexible-body swimming motions", Ph.D. dissertation, Massachusetts Institute of technology, June 1999.

[19] J-Y. Cheng and G. L. Chahine, "Computational hydrodynamics of animal swimming : boundary element method and three-dimensional vortex wake structure", *Comparative Biochemistry and Physiology*, vol. 131, pp. 51-60, 2001.

[20] S. F. Galls and O. K. Rediniotis, "Computational simulation of the autonomous navigation of a biomimetic underwater vehicle", *AIAA Jounal*, vol. 41, pp. 605-611, 2003.

[21] G. I. Taylor, "Analysis swimming long narrow animals", *Proc. of the Royal Society of London, series A : Mathematical and physical sciences*, vol. 214, pp. 158-183, 1952.

[22] J. Lighthill, "Note on the swimming of slender fish", *J. Fluid Mechanics*, vol. 9, pp. 305-307, 1960.

[23] J. Lighthill, "Hydromechanics of aquatic animal propulsion - A survey", *Annual review of fluid mechanics*, vol. 1, pp. 413-446, 1969.

[24] J. Lighthill, "Aquatic animal propulsion of high hydro-mechanical efficiency", *J. Fluid Mechanics*, vol. 44, pp. 265-301, 1970.

[25] J. Lighthill, "Large-amplitude elongated body theory of fish locomotion", *Proc. of Royal Society of London, Series B : Biological Sciences*, vol. 179, pp. 125-138, 1971.

[26] T. Y-T. Wu, "Swimming of a waving plate", *J. Fluid Mechanics*, vol. 10, pp. 321-355, 1961.

[27] S. D. Kelly and R. M. Murray, "Modeling efficient pisciform swimming for control", *J. Nonlinear and Robust Control*, vol. 10, pp. 217-241, 2000.

[28] E. Kanso, J. E. Marsden, C. W. Rowley and J. Melli-Huber, "Locomotion of articulated bodies in a perfect planar fluid", *J. of Nonlinear Science*, vol. 15, pp. 255-289, 2005.

[29] J. B. Melli, C. W. Rowley and D. S. Rufat, "Motion planning for an articulated body in a perfect fluid", *SIAM J. on applied dynamical systems*, vol. 5, pp. 650-669, 2006.

[30] T. McMillen and P. Holmes, "An elastic rod model for anguilliform swimming", *J. of Mathematical Biology*, vol. 53, pp. 843-886, 2006.

[31] H. Glauert, *The element of aerofoil and airscrew theory (second edition)*, Cambridge University Press, 1947.

[32] M. M. Munk, "The aerodynamic forces on airship hulls", *National Advisory Committee for Aeronautics*, report no. 184, 1924. [online]. Available : http ://naca.central.cranfield.ac.uk/reports/1924/naca-report-184.pdf

[33] E. D. Tytell and G. V. Lauder, "The hydrodynamics of eel swimming. I- Wake structure", *J. Experimental Biology*, vol. 207, pp. 1825-1841, 2004.

[34] E. D. Tytell, "The hydrodynamics of eel swimming. II- Effect of swimming speed", *J. Experimental Biology*, vol. 207, pp 3265-3279, 2004.

[35] G. Kirchhoff, "Ueber die Bewegung eines rotationskörpers in einer flüssigkeit", *J. für die reine und angewandte Mathematik*, vol.71, pp. 237-262, 1869.

[36] E. Cosserat and F. Cosserat, *Théorie des corps déformables*, Hermann, 1909.

[37] E. Reissner, "On a one-dimensional large displacement finite-strain theory", *Studies in Applied Mathematics*, vol.52, pp. 87-95, 1973.

[38] J. C. Simo and L. Vu-Quoc, "On the dynamics in space of rods undergoing large motions. A Geometrically Exact Approach", *Computer Methods in Applied Mechanics Engineering*, vol. 66, pp. 125-161, 1988.

[39] F. Boyer and D. Primault, "Finite element of slender beams in finite transformations - A geometrically exact approach", *Int. J. for Numerical Methods in Engineering*, vol. 59, pp. 669-702, 2004.

[40] F. Boyer, M. Porez and W. Khalil, "Macro-continuous computed torque algorithm for the three-dimensional eel-like robot", *IEEE Trans. on Robotics*, vol. 22, pp. 763-775, 2006.

[41] F. Boyer and D. Primault, "The Poincaré-Chetayev equations and flexible multibody systems", J. of Applied Mathematics and Mechanics, vol. 69, pp. 925-942, 2005.

[42] W. Khalil, G. Gallot and F. Boyer, "Dynamic modeling and simulation of a 3-D serial eel-like robot" ; *IEEE Trans. on Systems, Man and Cybernetics - Part C : Applications and Reviews*, vol. 37, pp. 1259-1268, 2007.

[43] M. Alamir, M. El-Rafei, G. Hafidi, N. Marchand, M. Porez and F. Boyer, "Feedback design for 3D movement of an eel-like robot", *IEEE Int. Conf. on Robotics and Automation*, Rome, Italia, 2007, pp. 256-261.

[44] H. Lamb, *Hydrodynamics*, Dover Publication, 1932.

[45] S. F. Hoerner, *Fluid dynamics drag*, Hoerner Fluid Dynamics, 1965.

[46] J. Y. S. Luh, M. W. Walker and R. C. P. Paul, "On-line computational scheme for mechanical manipulator", *Trans. of ASME J. of Dynamic Systems, Measurement, and Control*, vol. 102, pp. 69-76, 1980.

[47] R. Featherstone, "The calculation of robot dynamics using articulated-body inertias", *Int. J. of Robotics Research*, vol. 2, pp 13-30, 1983.

[48] F. Boyer and W. Khalil, "An efficient calculation of flexible manipulator inverse dynamics", *Int. J. of Robotic Research*, vol. 17, pp. 282-293, 1998.

[49] D. C. Wilcox, *Turbulence modeling for CFD*, Second Edition, DCW Industries Inc., address : 5354 Palm Drive, La Cañada, California, 2002.

[50] H..K. Tennekes and J.L. Lumley, *A first course in turbulence*, MIT Press, 1983.

[51] R. Duvigneau and M. Visonneau, "Optimization of a Synthetic Jet Actuator for Aerodynamic Stall Control", *Computer & Fluids*, vol.35, issue 6, pp. 624-638, 2006.

[52] P. Queutey and M. Visonneau, "An Interface Capturing Method for Free-Surface Hydrodynamic Flows", *Computer & Fluids*, vol.36, issue 9, pp. 1481-1510, 2007.

[53] A. Hay, A. Leroyer & M. Visonneau, "H-adaptive Navier-Stokes simulations of free-surface flows around moving bodies", *J. Marine Science and Technology*, Vol.11, Issue 1, pp 1-18, 2006.

[54] J. H. Ferziger and M. Perić, *Computational methods for fluid dynamics*, 3rd Edition, Springer Verlag, Berlin - New York, 2002.

[55] J. R Canavin and P. W Likins, "Floating reference frames for flexible spacecraft", *AIAA 15th. Aerospace Sciences Meeting*, Los Angeles, USA, 1977, pp. 66-77.

[56] T. Sarpkaya, "Force on a circular cylinder in viscous oscillatory flow at low Keulegan-Carpenter numbers", *J. of fluid mechanics*, vol. 133, pp. 265-285, 1986.

[57] M. J. Ringuette, "Vortex formation and drag on low aspect ratio, normal flat plates", Ph.D. dissertation, California Institute of technology, Pasadena, California, 2004.

[58] J. Gray, "Studies in animal locomotion. I. The movement of fish with special reference to the eel", *J. Experimental Biology*, vol. 10, pp. 88-104, 1933.

[59] D. Weihs, "Hydrodynamical analysis fish turning manoeuvres", *Proc. of the Royal Society of London, series B : Biological Sciences*, vol. 182, pp. 59-72, 1972.

[60] K. D'Aout and P. Aerts, "A kinematic comparison of forward and backward swimming in the eel Anguilla Anguilla", *J. Experimental Biology*, vol. 202, pp. 1511-1521, 1999.